New Journal of Physics
The open-access journal for physics

Regimes of classical transport of cold gases in a two-dimensional anisotropic disorder

L Pezzé, M Robert-de-Saint-Vincent[1], T Bourdel, J-P Brantut[2], B Allard, T Plisson, A Aspect, P Bouyer and L Sanchez-Palencia[3]

Laboratoire Charles Fabry—UMR 8501, Institut d'Optique, CNRS, Univ Paris-Sud 11, 2 avenue Augustin Fresnel, F-91127 Palaiseau cedex, France
E-mail: laurent.sanchez-palencia@institutoptique.fr

New Journal of Physics **13** (2011) 095015 (34pp)
Received 7 March 2011
Published 26 September 2011
Online at http://www.njp.org/
doi:10.1088/1367-2630/13/9/095015

Abstract. We numerically study the dynamics of cold atoms in a two-dimensional disordered potential. We consider an anisotropic speckle potential and focus on the classical dynamics, which is relevant to some recent experiments. Firstly, we study the behavior of particles with a fixed energy and identify different transport regimes. At low energy, the particles are classically localized due to the absence of a percolating cluster. At high energy, the particles undergo normal diffusion, and we show that the diffusion coefficients scale algebraically with the particle energy, with an anisotropy factor that is significantly different from that of the disordered potential. At intermediate energy, we find a transient sub-diffusive regime, which is relevant to the time scale of typical experiments. Secondly, we study the behavior of a cold atomic gas with an arbitrary energy distribution, using the above results as the groundwork. We show that the density profile of the atomic cloud in the diffusion regime is strongly peaked and, in particular, that it is not Gaussian. Its behavior at large distances allows us to extract the energy-dependent diffusion coefficients from experimental density distributions. For a thermal cloud released into the disordered potential, we show that our numerical predictions are in

[1] Current address: Physikalisches Institut, Universität Heidelberg, Philosophenweg 12, 69120 Heidelberg, Germany.
[2] Current address: Institute for Quantum Electronics, ETH Zürich, Hönggerberg, CH-8093 Zürich, Switzerland.
[3] Author to whom any correspondence should be addressed.

agreement with experimental findings. Not only does this paper give insights into recent experimental results, but it may also help in the interpretation of future experiments searching for deviation from classical diffusion and traces of Anderson localization.

Contents

1. Introduction

Transport processes are widespread and commonly occur in many fields of physics, chemistry and biology, and have drawn the attention of both theorists and experimentalists. The diffusion of waves and particles in disordered media determines the behavior of a variety of physical systems. These include electronic conductivity in dirty materials [1], superfluidity of liquid helium in porous substrates [2] and diffusion of light in dense media [3], with applications in dielectric materials [4] or interstellar clouds [5]. Diffusion is at the heart of transport phenomena in most systems of condensed-matter physics. For instance, it underlies the Drude theory of conductivity [6], as well as the self-consistent theory of Anderson localization [7]. A major hindrance to the complete understanding of condensed-matter systems is the complex interplay of many relevant ingredients, such as the structure and thermal fluctuations of the underlying substrate [6], the disorder [8] and the inter-particle interactions, which can lead to either superconductivity [9] or metal–insulator transitions [10, 11]. This poses a number of fundamental questions regarding the existence and nature of disorder-induced metal–insulator transitions [12], the role of the spatial dimension and the effect of nonlinearities.

Currently, there is much attention being devoted to disordered quantum gases [13–17]. These systems offer unprecedented control of most parameters, including temperature,

geometry and particle–particle interactions [18–21]. Moreover, disordered potentials can be engineered almost at will, and their statistical properties can be controlled and tuned [22]. So far, a large body of theoretical work has been devoted to Anderson localization of non-interacting particles [23–35], interacting Bose [36–47, 95, 96] and Fermi [48–51] disordered gases and two-component disordered systems [52–58]. Experimentally, classical suppression of the transport of Bose–Einstein condensates [59, 60] and Anderson localization of matter waves [61, 62] in one dimension (1D) have been reported recently. The competition between interaction and disorder has been investigated in 1D bi-chromatic optical lattices [63, 64] and in three-dimensional (3D) disordered lattices [65, 66].

Studying the dynamics of even non-interacting atoms in a disordered potential is a difficult problem, especially in dimensions higher than one. For classical particles, the motion in disordered potentials is generally chaotic, which sparks a variety of dynamical regimes [67], including classical localization, normal diffusion as well as sub and super-diffusion. For waves, diffusion is obtained in the limit of incoherent multiple scattering [7, 68, 75, 76]. Multiple coherent scattering [68–70] from the random defects can induce weak [72] or strong [29] localization effects. With a view to searching for localization effects in cold atomic gases, characterization of classical transport regimes is a central task. It is of special interest in dimension two (2D), which is the marginal dimension for return probability in Brownian motion and for Anderson localization [71]. In the context of cold atomic gases, diffusion has been experimentally studied in random dissipative 3D optical molasses [73, 74] and conservative 2D random potentials [77].

In this paper, we numerically study the transport properties of cold atoms in 2D disorder. We consider a speckle potential and focus on the classical regime such that

$$\lambda_{\mathrm{dB}} \ll \sigma_{\mathrm{R}} \leqslant l_{\mathrm{B}} \ll L \ll L_{\mathrm{loc}}, \tag{1}$$

where σ_{R} is the characteristic length scale of the disordered potential, λ_{dB} is the atomic de Broglie wavelength, l_{B} is the Boltzmann (transport) mean free path, L is the system size and L_{loc} is the localization length. The inequality $\lambda_{\mathrm{dB}} \ll l_{\mathrm{B}}$ guarantees that wave interference effects, which are important in 2D, occur on a very large scale, which will be assumed here to be much larger than the system size and thus disregarded. In particular, besides the fact that, in 2D, all quantum states are localized [71], the inequality $L \ll L_{\mathrm{loc}}$ allows us to neglect strong localization effects. When neglecting wave interference effects, the main dynamical regime is provided by diffusion [3, 7]. For $\sigma_{\mathrm{R}} \leqslant l_{\mathrm{B}}$ (which is most often true), the condition $\sigma_{\mathrm{R}} \lesssim \lambda_{\mathrm{dB}}$ may be fulfilled. In this case, the wave nature of the particles governs the scattering from each defect. Here, instead we consider the opposite condition $\lambda_{\mathrm{dB}} \ll \sigma_{\mathrm{R}}$, meaning that the atoms scatter in the disordered potential as purely classical particles, hence satisfying the Newton equations of motion. Finally, since l_{B} is the typical length of ballistic trajectories, the inequality $l_{\mathrm{B}} \ll L$ ensures that the number of scattering events in the system is sufficiently large to strongly affect the motion of particles. As discussed in our previous paper, the regime indicated by equation (1) is relevant to some recent cold-atom experiments [77].

The central aim of this paper is to analyze the transport regimes of classical particles at different energies. In particular, we show that they strongly depend on the topographic properties of the disordered potential. An additional aim is to use these results to determine the behavior of atomic clouds with a broad energy distribution, as is relevant to cold-atom experiments.

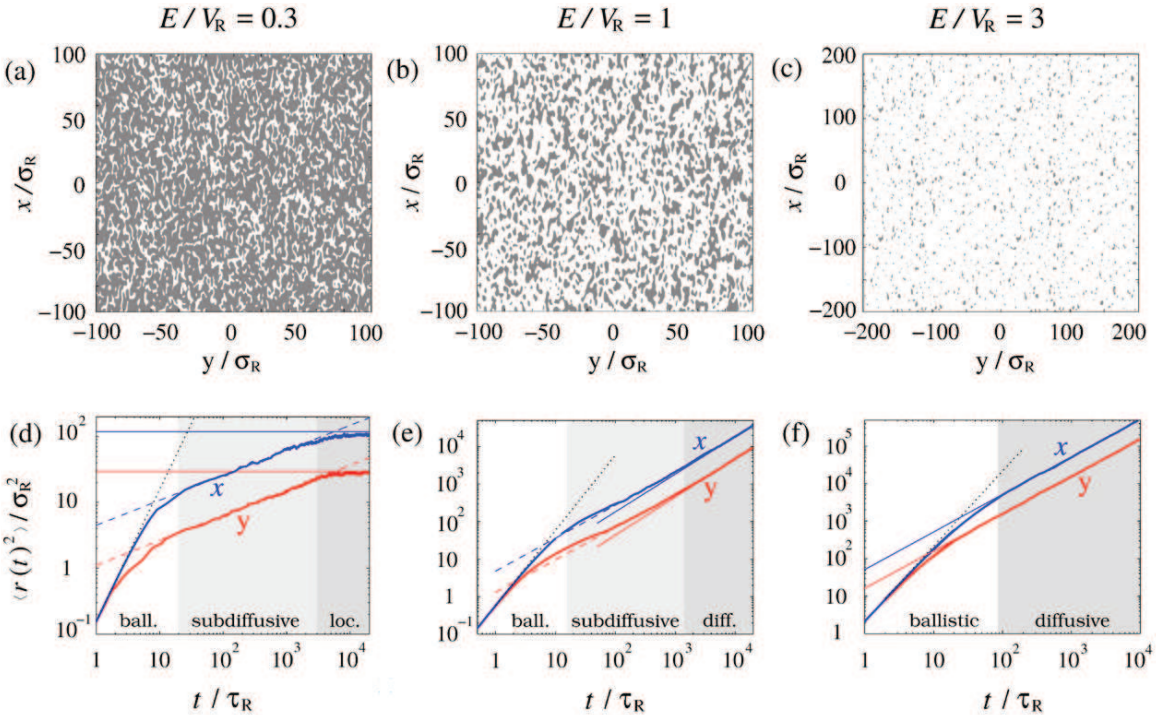

Figure 1. Topography and transport regimes of classical particles in a 2D, anisotropic, blue-detuned speckle potential with the anisotropy factor $\lambda = \sigma_x/\sigma_y = 2$ (see section 2.1). Panels (a)–(c) show the allowed (white; $V(\mathbf{r}) \leqslant E$) and forbidden (black; $V(\mathbf{r}) > E$) regions for a classical particle of energy E in the disordered potential $V(\mathbf{r})$. Different columns correspond to the same realization of the disordered potential and different energies: (a, d) $E = 0.3V_R$; (b, e) $E = 1V_R$; (c, f) $E = 3V_R$, where V_R is the average amplitude of the disordered potential (see section 2.1). In panel (a), the energy is below the percolation threshold $E_c = 0.52V_R$ (for the 2D blue-detuned speckle potential used here, see section 2.2) and all the particles are classically localized. In panels (b) and (c), the energy is above the percolation threshold and there appear allowed regions connecting the opposite sides of the box. Panels (d)–(f) show the mean square displacement, $\langle r(t)^2 \rangle$ (the direction $r = x$ is represented by the upper thick blue line and $r = y$ by the lower thick red line) as a function of time in units of $\tau_R \equiv \sqrt{m\sigma_R^2/|V_R|}$, where m is the mass of the atoms (see section 3.1). The black dotted line is the isotropic ballistic behavior, $\langle r(t)^2 \rangle \propto t^2$, predicted by equation (14). The dashed lines are $\langle r(t)^2 \rangle \propto t^{\alpha_r}$ (see equation (13)) for intermediate time scales giving sub-diffusive behavior ($\alpha_r < 1$) in (d) and (e). The solid lines are $\langle r(t)^2 \rangle \propto t^{\alpha_r}$ for long times, giving a time-independent behavior ($\alpha_r = 0$) in (d) and a diffusive scaling ($\alpha_r = 1$) in (e) and (f).

1.1. The main results presented in this paper

Here, we give a general overview of the main results of this paper (leaving the details for the text). Figure 1 illustrates the results obtained for an anisotropic speckle potential of the

anisotropy factor $\lambda = \sigma_x/\sigma_y$, with σ_r being the correlation length in the $r \in \{x, y\}$ direction. At any energy, a particle first undergoes a ballistic flight for a typical time $\tau^* \sim l_B/v$, where v is its initial velocity. At a sufficiently small energy, E, all classically allowed regions in the disordered potential have a finite size (see figure 1(a)), and the particle remains classically localized in the region containing its initial position. For a particle initially at the origin, the disorder-averaged mean square displacement, $\langle r(t)^2\rangle \propto t^{\alpha_r}$, shows sub-diffusive behavior ($\alpha_r < 1$) at intermediate times, which corresponds to the random exploration by the particle of its classically allowed region. Once the full region is explored, $\langle r(t)^2\rangle$ saturates asymptotically in time ($\alpha_r = 0$) to a finite value (see figure 1(d)). Being of purely topographical nature, this behavior leads to $\langle x^2\rangle/\langle y^2\rangle = \lambda^2$. A critical energy E_c signals the percolation phase transition corresponding to the appearance of infinitely extended allowed regions. For E slightly above E_c, the percolating cluster (classically allowed region) is characterized by large lakes connected by narrow bottlenecks (see figure 1(b)) which pass through the saddle points of the disordered potential. The particle then spends long periods of time exploring a lake, with a similar dynamics to that described above, leading to the sub-diffusive behavior observed in figure 1(e) at intermediate (but experimentally relevant) times. For longer times and larger distances, the dynamics is dominated by rare but possible transitions between the lakes, which leads, asymptotically in time, to normal diffusion, $\langle r(t)^2\rangle = 2D_r t$. At larger energy, the lakes merge and the size of forbidden regions rapidly decreases (see figure 1(c)). Then, the dynamics is characterized by normal diffusion for $t > \tau^*$ (see figure 1(f)). In this regime, we identify a power-law behavior of the diffusion coefficients as a function of the particle energy and show that the anisotropy of diffusion significantly differs from the anisotropy of the disorder, $D_x/D_y \neq \lambda^2$.

It is worth noting that a sub-diffusion regime should not be viewed as a precursor of localization. In fact, we see in the example considered here that sub-diffusion can cross over to either localization (for $E \lesssim E_c$) or normal diffusion (for $E \gtrsim E_c$).

1.2. Outlook

This paper is organized as follows. In section 2, we acquaint the reader with the main statistical and topographic properties of the 2D speckle potential used in the paper. We identify a percolation phase transition and determine the critical exponent characterizing the divergence of the classical localization length. In section 3, we analyze the dynamics of non-interacting classical particles of given energy in the disordered potential. Firstly, we write down the classical equations of motion and, with a proper rescaling, we highlight the universality class of the classical dynamics. Due to the redistribution of kinetic and potential energies induced by the disordered potential, the total particle energy is identified as the sole relevant parameter for the dynamics. Different transport regimes are then identified and discussed: (i) classical localization, (ii) normal diffusion and (iii) transient subdiffusion. Secondly, in section 4, we use the above results as the groundwork to study the overall dynamics of atomic gases with a broad energy distribution, as is relevant to cold-atom experiments. In particular, we show that, in the diffusion regime, the mean square size of the gas grows linearly in time ($\langle r(t)^2\rangle \propto t$) but, due to the summation of all diffusive components with energy-dependent diffusion coefficients, expanding density profiles significantly deviate from Gaussian functions. In section 5, considering a thermal cloud released in the disordered potential, we compare our predictions with the experimental results of [77]. We provide fitting functions to extract the

single-energy diffusion coefficients from the collective expansion of an atomic cloud of atoms. We find fair agreement between the numerical calculations and the experimental measurements. Finally, in section 6 we summarize our findings and discuss possible extensions of this work. On the one hand, our analysis provides a guideline for the experimental investigation of classical transport in cold-atomic gases in disordered potentials [77]. On the other, it may contribute to the interpretation of ongoing experiments searching for deviation from classical diffusion and traces of Anderson localization with ultracold gases in 2D geometry.

2. Disordered potential

2.1. Statistical properties of the speckle potential

Throughout this paper, we consider a speckle disorder, as commonly devised in cold-atom experiments [22, 59–61, 77–80]. A speckle pattern is created, for instance, by a coherent monochromatic laser beam passing through a diffusive plate [22]. A fully developed speckle field can be produced by a ground glass whose surface contains random grains associated with optical path length fluctuations longer than the laser wavelength. In this case, the speckle field, observed at the focal plane of a converging lens, results from the coherent superposition of waves originating from different scattering sites on the rough surface with uncorrelated phases uniformly distributed in $[0, 2\pi]$. Owing to the central limit theorem, the real and imaginary parts of the electric field are independent Gaussian variables. The light-shift potential $V(\mathbf{r})$ felt by the atoms exposed to the electromagnetic radiation is proportional to the field intensity: it is thus a random potential but we stress that its statistics is not Gaussian. The speckle potential is also inversely proportional to the detuning of the laser light with respect to the two-level atomic transition and can be either attractive or repulsive (see below). Finally, assuming a sufficiently far-detuned laser field, we will neglect dissipative effects in the following.

The statistical properties of the speckle potential have been extensively investigated [81]. The probability that the potential, at a given point $\mathbf{r}$, has amplitude $V \equiv V(\mathbf{r})$ follows an exponential law

$$P(V) = \frac{\mathrm{e}^{-V/V_\mathrm{R}}}{|V_\mathrm{R}|}\,\Theta\Big(\frac{V}{V_\mathrm{R}}\Big), \tag{2}$$

where Θ is the Heaviside step function. We have $\langle V(\mathbf{r})\rangle = V_\mathrm{R}$ and $(\Delta V(\mathbf{r}))^2 \equiv \langle V(\mathbf{r})^2\rangle - \langle V(\mathbf{r})\rangle^2 = V_\mathrm{R}^2$, where $\langle\cdots\rangle$ indicates the average over the different realizations of the disordered potential. The quantity V_R is the amplitude of the disorder, and its sign depends on the detuning of the laser light from the atomic resonance: for a blue-detuned speckle potential, the disorder is repulsive (i.e. positive $V_\mathrm{R} > 0$ and $V(\mathbf{r}) \geqslant 0$) and is characterized by arbitrary large-intensity peaks with an exponentially low probability. Conversely, for a red-detuned speckle potential, the disorder is attractive (i.e. negative $V_\mathrm{R} < 0$ and $V(\mathbf{r}) \leqslant 0$) and is characterized by arbitrary low dips with an exponentially low probability.

The autocorrelation function of the disordered potential, $C(\mathbf{r}) = \langle V(\mathbf{r}+\mathbf{r}')V(\mathbf{r}')\rangle - \langle V(\mathbf{r}')\rangle^2$, can be controlled by the geometry of the diffusive plate [22]. Without loss of generality, it can be written as $C(\mathbf{r}) = V_\mathrm{R}^2 c(\mathbf{r}/\sigma_\mathrm{R})$, where σ_R is the correlation length of the disordered potential, i.e. the typical width of $C(\mathbf{r})$, which is proportional to the speckle grain size[4]. The precise definition of σ_R depends on the specific model of disorder. In this paper, we

[4] Note that $c(0) = 1$.

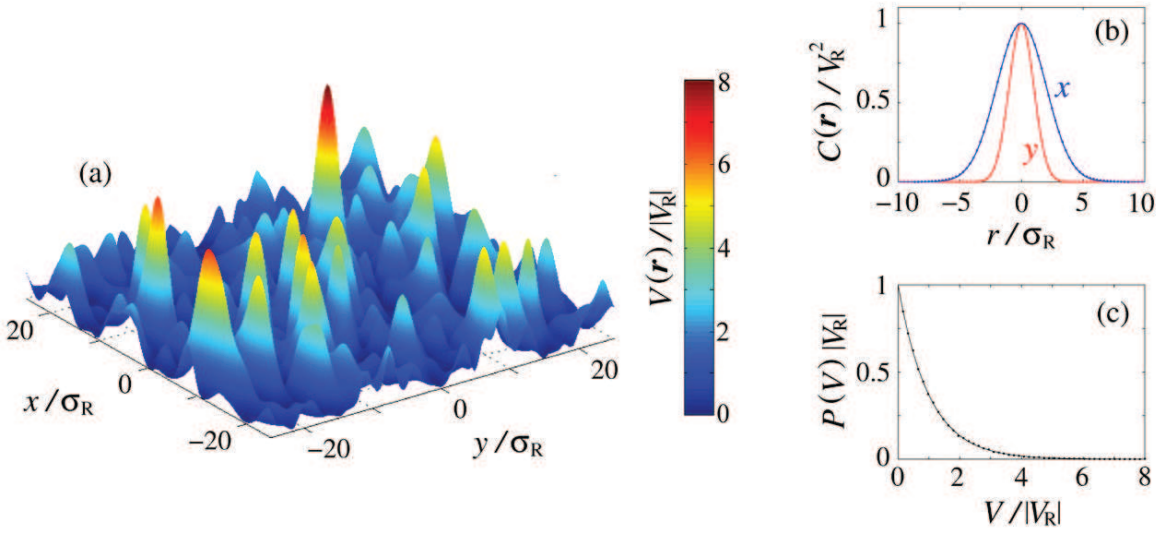

Figure 2. (a) Example of the anisotropic speckle potential used in numerical simulations. The anisotropy factor is $\lambda = \sigma_x/\sigma_y = 2$. (b) Autocorrelation function of the disordered potential (dots), along the x- and y-directions ($C(x, y = 0)$ and $C(x = 0, y)$, respectively). It has been obtained numerically by averaging over 100 000 realizations of the disordered potential. The solid lines correspond to equation (3) with no fitting parameters. (c) Intensity distribution obtained for a single realization of the disordered speckle potential (dots). The solid line is equation (2).

focus on a 2D, anisotropic, speckle potential with a Gaussian correlation function of widths σ_x and σ_y along the two main directions,

$$C(\mathbf{r}) = V_R^2 \exp(-x^2/2\sigma_x^2) \exp(-y^2/2\sigma_y^2). \tag{3}$$

We define $\sigma_R \equiv \sigma_x$ and $\lambda \equiv \sigma_x/\sigma_y$ is the anisotropy factor. In figure 2(a), we show a typical realization of a speckle potential as used in the numerical simulations ($\lambda = 2$). Figures 2(b) and (c) show its autocorrelation function and intensity distribution, respectively. Experimentally, a speckle potential with a Gaussian correlation function can be obtained by illuminating a diffusive plate with a Gaussian laser beam. The anisotropy can be controlled by the aperture function of the diffusive plate [22, 81] or by tilting a 2D, isotropic speckle field with respect to the diffusion plane of the atoms [77].

2.2. Topographic properties of the speckle potential

We now study some topographic properties of the 2D speckle potential that are relevant for understanding the transport regimes of classical particles (see section 3). Some of them, such as, for instance, the percolation threshold, which will be discussed below, do not depend on the anisotropy of the potential. These are thus straightforwardly obtained from those of the isotropic case upon rescaling of the y-direction by the anisotropy factor λ. We thus focus, without loss of generality, on an isotropic speckle disorder in this subsection.

The positivity of the kinetic energy constrains the trajectories of classical particles with total energy E to the sub-space defined by $V(\mathbf{r}) \leqslant E$. This condition separates the space in allowed and forbidden regions. For the sake of illustration, figures 1(a)–(c) show the classically allowed ($V(\mathbf{r}) \leqslant E$; white) and forbidden ($V(\mathbf{r}) > E$; black) regions for particles of fixed energy in a specific realization of a 2D blue-detuned anisotropic speckle potential. In a continuous disordered potential, the topography of classically allowed regions strongly depends on the ratio $E/|V_R|$ and, for a speckle potential, on the sign of V_R. The fraction of space satisfying the condition $V(\mathbf{r}) \leqslant E$ is given by [82]

$$\phi(E) = \int_{-\infty}^{E} \mathrm{d}V\, P(V). \tag{4}$$

For a speckle potential, $P(V)$ is given by equation (2). For blue-detuned speckle potentials, we thus find $\phi(E) = 1 - \mathrm{e}^{-E/|V_R|}$ for $E \geqslant 0$ and $\phi(E) = 0$ (i.e. there is no allowed region) for $E \leqslant 0$. For red-detuned speckle potentials, we have $\phi(E) = \mathrm{e}^{+E/|V_R|}$ for $E \leqslant 0$ and $\phi(E) = 1$ (i.e. there are no forbidden regions) for $E \geqslant 0$.

For 2D disordered potentials, there exists a critical energy, the so-called *percolation threshold*, E_c, which marks the sharp transition between the existence of infinitely extended allowed and forbidden regions [82]. The *percolation transition* is often considered as the simplest possible phase transition with nontrivial critical behavior (for a review, see [83]). It has a pure geometrical nature and exhibits long-range correlation near the critical value, corresponding to the divergence of the average size of the allowed regions (in infinite space).

Below E_c, the allowed regions are disconnected and form 'lakes' of finite size (see figure 1(a)). The allowed regions consist of a finite number of minima of the potential, which are connected through saddle points. In other words, particles of energy $E \leqslant E_c$ are classically localized, i.e. they cannot move to arbitrary long distances. On a macroscopic scale, the system behaves as an insulator. Above E_c, an infinite number of 'lakes' merge together to form an infinite 'ocean': the allowed subspace contains at least one connected subset (cluster) which stretches to infinity (see figures 1(b) and (c)). In other words, particles with energy $E > E_c$ and initially placed in an infinitely extended allowed region can move to infinity. The system thus behaves as a conductor.

A challenging issue is to determine the value of the percolation threshold E_c for different models of disorder. In the case of a disordered potential with sign symmetry, (i.e. when the statistical properties of the potential $V(\mathbf{r})$ are equivalent to those of $2\langle V(\mathbf{r})\rangle - V(\mathbf{r})$), the percolation threshold $E_c = \langle V(\mathbf{r})\rangle$ and the corresponding critical area fraction is $\phi_c \equiv \phi(E_c) = 1/2$ [82]. An example is given by Gaussian random distributions. However, a speckle potential is non-Gaussian and does not have the sign symmetry discussed above. For instance, a blue-detuned speckle potential is bounded below by zero, but it is unbounded above (and vice versa for the red-detuned speckle potential). We have numerically investigated the percolation threshold in 2D speckle potentials with the correlation function given by equation (3) with $\lambda = 1$. In particular, we have evaluated the probability (for different realizations of the disorder), P_{perc}, of having an allowed region connecting the opposite sides of a square box. The results are shown in figure 3 for a blue-detuned speckle and for different box lengths, L. As expected, the crossover between $P_{\mathrm{perc}} = 0$ and $P_{\mathrm{perc}} = 1$ becomes sharper and sharper with increasing L, and all curves cross the value $P_{\mathrm{perc}} = 0.5$ at approximately the same value of E/V_R. This is compatible with a phase transition at $E_c = 0.52V_R$, for a blue-detuned, 2D, speckle potential, in the limit $L \to \infty$ (the vertical dashed line in the figure). According to equation (4), the

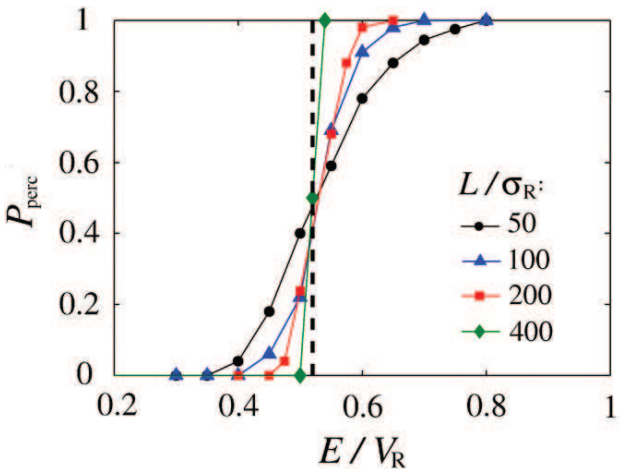

Figure 3. Percolation probability as a function of the particle energy. It is calculated numerically as the probability of finding at least one allowed region connecting the opposite sides of a square box of size L in a blue-detuned (isotropic) speckle potential. Different symbols correspond to different values of L (indicated in the figure) and the solid lines are a guide to the eyes. The vertical dashed line indicates the percolation threshold, $E_c = 0.52V_R$. The percolation probability is calculated over 100 realizations of the disorder and the numerical grid step is $\sigma_R/10$.

critical fraction of allowed regions is given by $\phi_c = 0.405$, a value significantly different from 0.5 as expected for potentials with sign symmetry. The values $E_c = 0.52V_R$ and $\phi_c = 0.405$ found here are in agreement with the experimental findings [84] and numerical results [85] obtained by mapping the speckle potential onto a network connecting potential minima through saddle points (see also [97]). Because of the duality between allowed and forbidden regions in the 2D case, when inverting the sign of the potential, allowed regions for a particle of energy E become forbidden regions for a particle of energy $-E$. The percolation threshold for the red-detuned speckle potential can then be directly calculated from that of the blue-detuned speckle potential: $E_c(-V_R) = -E_c(V_R)$. For red-detuned speckle potentials, we thus find that the percolation threshold is $E_c = -0.52|V_R|$ and the corresponding fraction of allowed regions is $\phi_c = 0.595$.

In order to further characterize the topographic properties of the speckle potential in a homogeneous box, we have studied the classical localization length $\mathscr{L}(E)$, i.e. the mean diameter of the percolating cluster stretching from the box center. We use the definition

$$\mathscr{L}(E) \equiv 2\sqrt{\delta \mathbf{r}^2}, \tag{5}$$

where $\delta \mathbf{r}^2 = \int \mathrm{d}^2\mathbf{r}\, A_E(\mathbf{r})|\mathbf{r}|^2 / \int \mathrm{d}^2\mathbf{r}\, A_E(\mathbf{r})$ with $A_E(\mathbf{r}) = 1$ in the classically allowed region stretching from the box center (if $V(\mathbf{r} = 0) \leqslant E$) and $A_E(\mathbf{r}) = 0$ elsewhere. The calculation of the localization length, equation (5), at a fixed energy is repeated for several realizations of the disordered potential. The corresponding probability distribution $P_E(\mathscr{L})$ is shown in figure 4(a) for various energies. It decreases exponentially for sufficiently large values of $\mathscr{L}$.

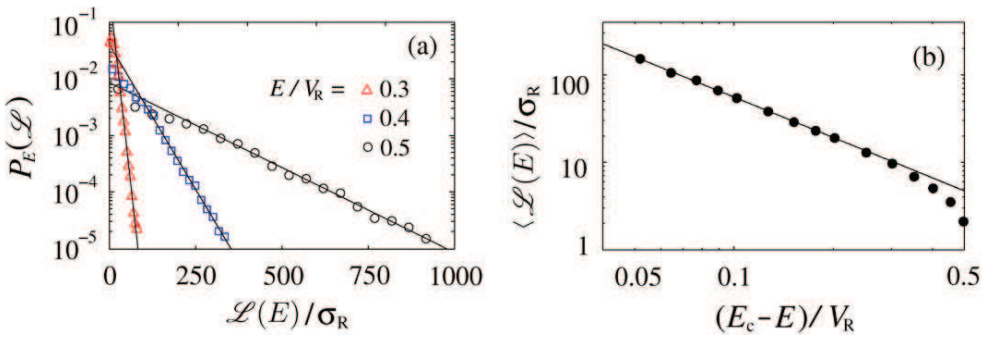

Figure 4. (a) Probability distribution of the classical localization length defined in equation (5), for a blue-detuned speckle potential. Symbols are the numerical results for different energies (indicated in the figure). The solid lines are fits to an exponential function. For instance, for $E = 0.3V_R$ (triangles), the fit gives $P_E(\mathscr{L}) \simeq (0.35/\sigma_R)\ \exp(-0.12\,\mathscr{L}/\sigma_R)$ for $\mathscr{L} \gtrsim 30\sigma_R$. (b) Average localization length as a function of $E_c - E$. The line is a fit to equation (6) where a, E_c and ν_c are the fitting parameters. The numerical results (dots) have been obtained after averaging over 100 00 realizations of a blue-detuned isotropic speckle potential in a box of length $L = 800\sigma_R$ with grid step $\sigma_R/8$.

The average localization length, $\langle \mathscr{L}(E) \rangle \equiv \int \mathrm{d}\mathscr{L}\, \mathscr{L} P_E(\mathscr{L})$ is shown in figure 4(b). It diverges when approaching the percolation threshold E_c and, close to this value, it can be well fitted to the function

$$\langle \mathscr{L}(E) \rangle = a\left(\frac{E_c - E}{V_R}\right)^{-\nu_c}, \tag{6}$$

where $a = 1.63 \pm 0.3\,\sigma_R$, the critical exponent $\nu_c = 1.53 \pm 0.2$ and the percolation threshold $E_c = 0.54 \pm 0.02$ are fitting parameters. The value of E_c obtained from the fit is in agreement, within the numerical error, with the value $E_c = 0.52V_R$ found by other methods (see figure 3).

Above the percolation threshold, for $E > E_c$, not all the allowed energy regions extend to infinity and some particles can still be classically localized, depending on their initial position. This behavior is relevant to our system, where the dynamics starts *inside* the disordered potential. We have thus studied, as a function of the particle energy, the probability P_R of finding, for different realizations of the disordered potential, an allowed region connecting two points at a distance $R = \sqrt{x^2 + y^2}$. The results are shown in figures 5(a) and (b) for the blue- and red-detuned speckle potentials, respectively. For a large enough distance R, the probability shows a sharp transition, from zero, for $E \leqslant E_c$, to a finite value, for $E > E_c$. Note that, for $E > E_c$, the probability converges to a curve that does not depend on the length R. This is consistent with the existence of allowed regions of finite size above the percolation threshold. The number of such regions rapidly decreases with increasing energy. In a blue-detuned speckle potential (see figure 5(a)), there are always forbidden regions but, for energy $E \gtrsim V_R$, almost all percolation regions extend to infinity (P_R quickly approaches the value 1). In a red-detuned speckle potential (see figure 5(b)) there is a single percolation region for $E > 0$, as there is no forbidden region in this case.

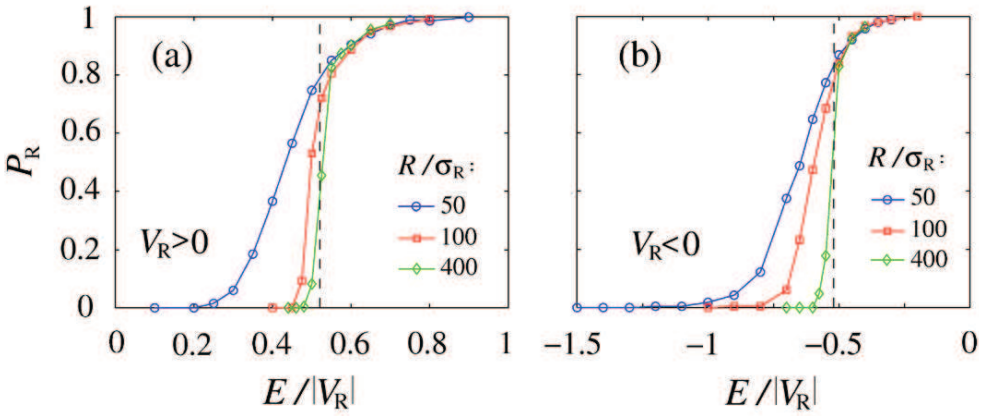

Figure 5. Probability for finding a classically allowed region stretching to a distance larger than R. Each point has been obtained after averaging over 500 realizations of the disordered potential. Different lines refer to different values of R (indicated in the figure). Panels (a) and (b) correspond to blue- and red-detuned speckle potentials, respectively. The vertical dashed lines are the percolation threshold $E_c = 0.52V_R$.

3. Transport regimes in a two-dimensional disordered potential

In this section, we study the dynamics of a classical particle of a fixed total energy E in a 2D anisotropic disorder. The central goal is to characterize the behavior of the mean square displacement as a function of the particle energy. We mainly focus on blue-detuned speckle potentials but also discuss the results for the red-detuned case.

3.1. Classical equations of motion

The dynamics of a classical particle in a disordered potential is most conveniently written by rescaling the dynamical variables in the following way:

$$\tilde{E} = E/|V_R|, \tag{7a}$$

$$\tilde{\mathbf{r}} = \mathbf{r}/\sigma_R, \tag{7b}$$

$$\tilde{\mathbf{p}} = \mathbf{p}/p_R, \tag{7c}$$

$$\tilde{t} = t/\tau_R, \tag{7d}$$

where E is the particle energy, $\mathbf{r} = (x, y)$ its position, $\mathbf{p} = (p_x, p_y)$ its momentum and t is the time. Introducing the momentum $p_R = \sqrt{m|V_R|}$ and the time $\tau_R = \sqrt{m\sigma_R^2/|V_R|}$, where m is the atomic mass, the classical equations of motion read

$$\frac{d\tilde{\mathbf{r}}}{d\tilde{t}} = \tilde{\mathbf{p}}, \tag{8a}$$

$$\frac{d\tilde{\mathbf{p}}}{d\tilde{t}} = -\frac{dv(\tilde{\mathbf{r}})}{d\tilde{\mathbf{r}}}, \tag{8b}$$

where $\upsilon(\tilde{\mathbf{r}}) = V(\mathbf{r})/|V_R|$ is the reduced disordered potential. Equations (8) highlight the universality class of the classical dynamics: upon the above rescaling by the disorder parameters V_R and σ_R, the classical dynamics only depends on the properties of the reduced potential, $\upsilon(\tilde{\mathbf{r}})$, i.e. on the model of disorder, and in particular on its anisotropy. It is then sufficient to study the particle dynamics for a single set of parameters V_R and σ_R. This is an important difference compared with the quantum dynamics, which also depends on V_R/E_R, where $E_R = \hbar^2/m\sigma_R^2$ [29, 87, 88].

The reduced equations (8), for the speckle potential described in section 2, form the basis of the calculations reported in this paper. For each realization of the disordered potential $V(\mathbf{r})$, we numerically solve equations (8) to calculate the classical phase-space trajectory $(\mathbf{r}(t), \mathbf{p}(t))$, depending on the initial conditions $(\mathbf{r}_0, \mathbf{p}_0)$. We use an adaptive ordinary differential equation algorithm where the time step is adjusted such that the energy is conserved within about 0.5% over the entire evolution. Numerical simulations are run with the fixed initial position $\mathbf{r}_0 = 0$. The initial momentum is chosen with amplitude $|\mathbf{p}_0| = \sqrt{2m[E - V(\mathbf{r}_0)]}$ and, unless otherwise specified, along a random direction chosen homogeneously. Disordered speckle potentials are randomly generated and disregarded if $V(\mathbf{r}_0) > E$. They are typically created in a box of linear length $L = 400\sigma_R$ with a grid step $\Delta x = \Delta y = \sigma_R/10$ and repeated periodically over the infinite plane[5]. Quantities of interest (see below) are then obtained by averaging over different realizations of the disordered potential.

3.2. Time scale of ballistic dynamics

The primary effect of the disordered potential is to modify the ballistic dynamics of particles. A particle of energy E initially moving along the $r \in \{x, y\}$ direction loses the memory of its initial momentum within a characteristic time scale $\tau_r^*(E)$.[6] In order to identify $\tau_r^*(E)$, we have studied the momentum covariance tensor

$$\mathrm{Cov}_{r,r'}(t) \equiv \langle\, p_r(t)\, p_{r'}(0)\,\rangle. \tag{9}$$

The typical behavior of the diagonal elements of the normalized momentum covariance, $\mathrm{Cov}_r(t) \equiv \mathrm{Cov}_{r,r}(t)/\langle p_r^2(0)\rangle$, is shown in figure 6(a) as a function of time and along the $r = x, y$ directions. We have checked that the off-diagonal elements of equation (9) vanish, in our case. The quantity $\mathrm{Cov}_r(t)$ is characterized by a rapid decay and we define $\tau_r^*(E)$ such that $\mathrm{Cov}_r[\tau_r^*(E)] = 0.1$. For an anisotropic speckle disorder, we find that $\tau_x^*(E) \neq \tau_y^*(E)$ and $\tau_r^*(E)$ increases with σ_r $(r \in \{x, y\})$. We then introduce $\tau^*(E) \equiv \min[\tau_x^*(E), \tau_y^*(E)]$. For times $t \lesssim \tau^*(E)$, the dynamics is ballistic and isotropic. For times $t \sim \tau^*(E)$, the dynamics is modified by the disorder; it enters various transport regimes and may become anisotropic (see section 3.4).

Note that, in our simulations, $\mathrm{Cov}_r(t)$ does not exactly converge to zero at large times as exemplified in figure 6(a). We indeed find fluctuations with both positive and negative values, which survive massive configuration averaging. We have, however, checked, from our numerical results that the integral $\mathrm{I}_r(t) \equiv \int_0^t \mathrm{d}u\, \mathrm{Cov}_{r,r}(u)/m^2$ converges in the long time limit to a finite value (up to fluctuations), as shown in figure 6(b). This holds for particles of energy both above and below the percolation threshold. In addition, for particles in the normal diffusion regime, the limit of this integral equals the diffusion coefficient obtained with the fit of the

[5] By numerical construction, the 2D speckle potential is continuous at the box boundaries.

[6] Alternatively, one can introduce the ballistic path length, $l_r^*(E) \equiv \tau_r^*(E)\sqrt{2E/m}$, which is the characteristic length traveled by a particle, beyond which its trajectory is affected by the disorder.

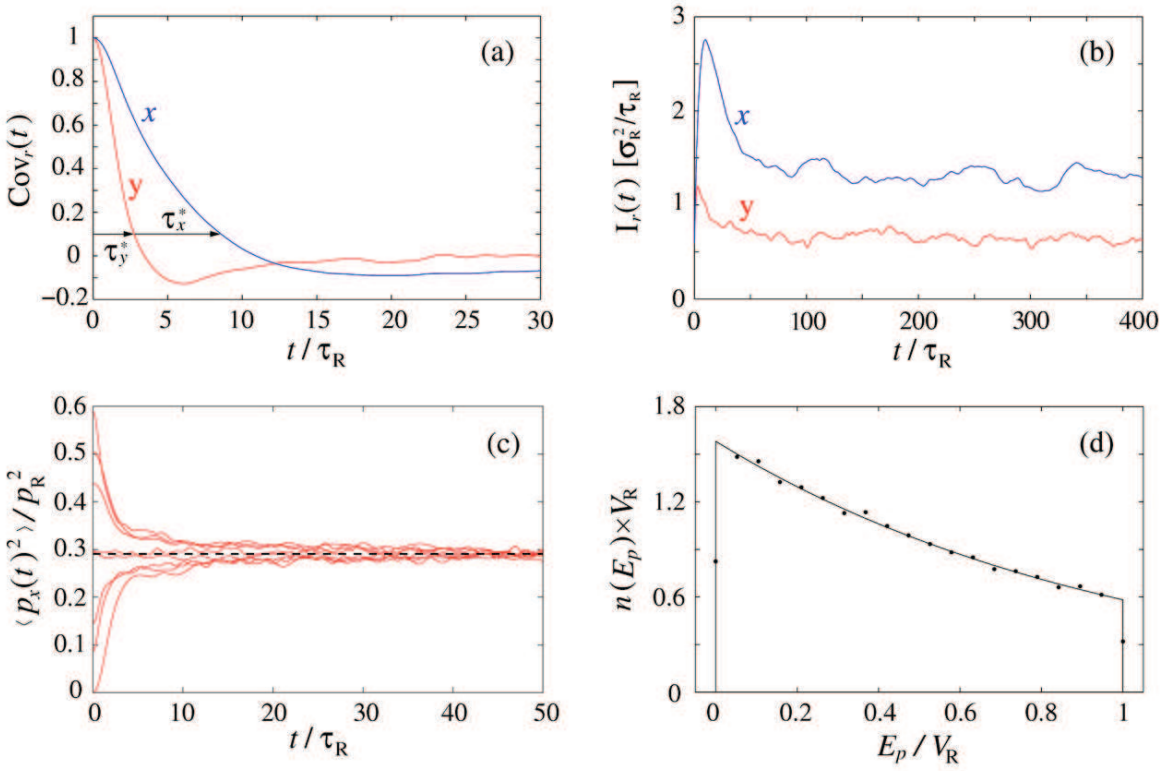

Figure 6. Primary effects of the disordered potential on the dynamics of a classical particle: modification of the ballistic dynamics and redistribution of energy. Here, we consider particles of energy $E = V_R$. Panel (a) shows the normalized momentum covariance $\mathrm{Cov}_r(t)$ for particles with momentum $p_r(0) = \sqrt{2m[E - V(\mathbf{r}_0)]}$ along the $r = x$ (blue line) and the $r = y$ (red line) direction, as a function of time. (b) Integral of the momentum covariance, $\mathrm{I}_r(t)$ (in units σ_R^2/τ_R), as a function of time and along the $r = x$ (blue line) and the $r = y$ (red line) direction. (c) Average kinetic energy, $\langle p_x(t)^2\rangle/2m$. The different solid lines refer to particles with a fixed energy and different initial momentum directions. The dotted line represents equation (12). Analogous results are obtained for $\langle p_y(t)^2\rangle/2m$. (d) Potential energy distribution obtained at time $t = 30\tau_R$. The dots are numerical results and the solid line represents equation (10). The numerical results have been obtained for a blue-detuned speckle potential ($V_R > 0$) by averaging over 10 000 realizations in panels (a) and (d) and 2000 realizations in panels (b) and (c).

mean square displacement as discussed in section 3.4. This is consistent with the celebrated relation, $D_{r,r'} = \int_0^{+\infty} \mathrm{d}t\ \mathrm{Cov}_{r,r'}(t)/m^2$, valid for normal diffusion [83], where $D_{r,r'}$ is the (r, r') component of the diffusion tensor.

3.3. Energy redistribution

Another main effect of disorder is to redistribute, after a time of the order of $\tau^*(E)$, the different forms (kinetic and potential) of the particle energy, under the constraint that the total energy

is conserved. An example is shown in figure 6(c) where we plot the average kinetic energy along the x-direction, $\langle p_x(t)^2\rangle/2m$, as a function of time. Different lines correspond to particles with the same energy $E = V_R$ and different initial momentum directions $\mathbf{p}_0$. After times of the order of $\tau^*(E)$, the lines converge to the same value, $\langle E_k\rangle$, which will be calculated below (see equation (12)).

A first insight into the dynamics is obtained by using the statistical micro-canonical ensemble, which assumes phase-space ergodicity in the shell of energy E. The probability distribution of the potential energy E_p for a particle of energy E in a single realization of the disordered potential is then $n(E_p) \propto \int d\mathbf{r}\, d\mathbf{p}\, \delta[E - \mathbf{p}^2/2m - V(\mathbf{r})]\, \delta[V(\mathbf{r}) - E_p]$. In a continuous, homogeneous disorder, averaging over realizations of the disordered potential equals spatial averaging, so that $\int d\mathbf{r}\, \delta[V(\mathbf{r}) - V] \propto P(V)$ [89].

For a blue-detuned speckle potential, using equation (2), we find that

$$n(E_p) = \frac{e^{-E_p/V_R}}{V_R(1 - e^{-E/V_R})}\Theta(E_p)\Theta(E - E_p), \quad V_R > 0, \tag{10}$$

normalized such that $\int dE_p\, n(E_p) = 1$. The distribution $n(E_p)$ is shown in figure 6(d) for $E = V_R > 0$. The good agreement between the numerical data (dots) and the analytic prediction (equation (10); solid line) legitimates the micro-canonical statistical model above and, consequently, the phase-space ergodicity hypothesis. Using equation (10), we find that the average potential energy of a particle of energy E in the disordered potential is

$$\langle E_p\rangle = V_R\left(1 - \frac{E/V_R}{e^{E/V_R} - 1}\right), \quad V_R > 0. \tag{11}$$

Then, using the relation imposed by energy conservation, $E = \langle E_k\rangle + \langle E_p\rangle$, we find that the average kinetic energy is given by

$$\langle E_k\rangle = V_R\left(\frac{E/V_R}{1 - e^{-E/V_R}} - 1\right), \quad V_R > 0. \tag{12}$$

In particular, in the limit $E \ll V_R$, we have $\langle E_p\rangle \simeq E/2$ and $\langle E_k\rangle \simeq E/2$. This is easily interpreted: the particles are trapped in minima of the disordered potential, which can be assimilated to local (2D) harmonic oscillators, and the total energy is equally partitioned over the four degrees of freedom. In the opposite limit, $E \gg V_R$, the energy of the particles strongly exceeds the disordered potential, the velocity field is nearly uniform and the average potential energy equals the spatial average of the disordered potential. We have $\langle E_p\rangle \simeq V_R$ and $\langle E_k\rangle \simeq E - V_R$. Finally, equation (12) is in excellent agreement with the asymptotic value of the kinetic energy obtained in numerical calculations (see figure 6(c)). For a red-detuned speckle potential, we find similar behavior. The counterparts of equations (10)–(12) have been calculated[7] and checked numerically.

[7] For a red-detuned speckle potential ($V_R < 0$), we find that

$$n(E_p) = \frac{e^{-E_p/V_R}}{|V_R|}\begin{cases} e^{E/V_R}\,\Theta(E - E_p), & \text{for } E \leqslant 0, \\ \Theta(E_p/V_R), & \text{for } E \geqslant 0. \end{cases}$$

For $E \leqslant 0$, the average values of the potential energy and of the kinetic energy along each direction are $\langle E_p\rangle = V_R + E$ and $\langle E_k\rangle = |V_R|$, respectively. For $E \geqslant 0$, we find that $\langle E_p\rangle = V_R$ and $\langle E_k\rangle = E + |V_R|$. The latter relations are intuitive in the limit $E \gg |V_R|$. The fact that they hold for $E \geqslant 0$ is a consequence of phase-space ergodicity in the 2D geometry.

3.4. Energy-dependent transport regimes

In the following, we study the mean square displacement, $\langle r(t)^2\rangle$, along the $r \in \{x, y\}$ direction. Note that, after disorder averaging, the two parity symmetries $x \leftrightarrow -x$ and $y \leftrightarrow -y$ of the 2D (anisotropic) speckle potential impose $\langle x(t)\rangle = \langle y(t)\rangle = \langle x(t)y(t)\rangle = 0$, for $t \gg \tau^*(E)$ when fixing the initial momentum direction. The above mean values hold at any time when averaging over an isotropic initial momentum distribution.

Figures 1(d)–(f) show the typical behavior of $\langle r(t)^2\rangle$ as a function of time, for three different energies E in a blue-detuned speckle potential ($V_R > 0$). Quite generally, the plots in the log–log scale show straight lines for long time periods. In each of them, the dynamics is well described by the general formula

$$\frac{\langle r(t)^2\rangle}{\sigma_R^2} = 2\tilde{D}_r \times \left(\frac{t}{\tau_R}\right)^{\alpha_r}, \tag{13}$$

where the parameters $\tilde{D}_r$ and α_r depend on the rescaled energy E/V_R. The different transport regimes are determined by the value of the exponent α_r: (i) classical localization ($\alpha_r = 0$), where $\langle r(t)^2\rangle$ is independent of time; (ii) sub-diffusion ($0 < \alpha_r < 1$); (iii) normal diffusion ($\alpha_r = 1$); (iv) super-diffusion ($1 < \alpha_r < 2$); (v) ballistic expansion ($\alpha_r = 2$), which holds for free particles.

As discussed above, for times $t \lesssim \tau^*(E)$, the dynamics is isotropic and ballistic. We have

$$\frac{\langle r(t)^2\rangle}{\sigma_R^2} = \bar{v}_0^2 \times \left(\frac{t}{\tau_R}\right)^2, \tag{14}$$

where $\bar{v}_0 = \sqrt{2\langle E_k\rangle_0/|V_R|}$ and $\langle E_k\rangle_0$ is the kinetic energy averaged over an isotropic momentum distribution. For the 2D geometry considered here, we have $\langle E_k\rangle_0 = \langle E_k\rangle$, which for a blue-detuned speckle potential is given by equation (12).[8] Equation (14) is the dotted black line in figures 1(d)–(f) and, as expected, shows very good agreement with the numerics (see footnote 6) for short times.

For longer times ($t \gg \tau^*(E)$), the dynamics is strongly affected by the disorder and we have $\alpha_r < 2$. In the following, we discuss the transport regimes accessible to the particles, depending on their energy.

3.4.1. Classical localization regime. Let us first discuss the dynamical behavior of a particle of energy below the percolation threshold ($E < E_c$). Figure 1(d) shows that, on average, $\langle r(t)^2\rangle$ is well described by equation (13), with different parameters in different time intervals. At intermediate times, the particle chaotically explores the finite-size allowed region to which it belongs, bouncing between the borders. Its probability distribution progressively fills this region and we then find subdiffusive behavior ($\alpha_r < 1$). At asymptotically large times, when the probability distribution has filled all the allowed region, we find that $\alpha_r = 0$, corresponding to

[8] We recall that, in the numerics, the particle is initially at the origin, $\mathbf{r} = 0$, with an isotropically distributed momentum direction. The total energy E is fixed and the disordered potential is randomly chosen and kept only if $E > V(\mathbf{0})$. The initial potential energy distribution is thus given by $n_0(E_p) \propto P(E_p)\Theta(E - E_p)$. The average initial kinetic energy is $\langle E_k\rangle_0 = E - \langle E_p\rangle_0$, where $\langle E_p\rangle_0$ is the average potential energy. For a blue-detuned speckle potential, an explicit calculation gives $\langle E_k\rangle_0 = V_R\left(\frac{E/V_R}{1-e^{-E/V_R}} - 1\right)$. For a red-detuned speckle, $\langle E_k\rangle_0 = |V_R|$ if $E \leqslant 0$ and $\langle E_k\rangle_0 = E + |V_R|$ if $E \geqslant 0$. Note that, in the 2D geometry, we find that $n_0(E_p)$ equals $n(E_p)$ as calculated in section 3.3. However, while $n_0(E_p)$ is obtained by averaging over the particle momentum direction, $n(E_p)$ is obtained in the micro-canonical ensemble model, where momentum averaging results from energy distribution.

classical localization. In this case, the coefficients $\tilde{D}_r$ in equation (13) are given by the average mean square size of the allowed regions along the x- and y-directions (these are plotted as horizontal solid lines in figure 1(d)). In an anisotropic disorder, we find that $\langle x^2\rangle/\langle y^2\rangle \simeq \lambda^2$, which is consistent with the fact that the allowed regions are anisotropic, with the same anisotropy factor as the potential.

In order to get further insight on the relation between this behavior and the topography of the allowed regions, we have studied the 'probability of diffusion', $f(\mathbf{r}, t|\mathbf{r}_0, t_0)$, which is the probability distribution to find a particle at position $\mathbf{r}$ at time t assuming that it is at position $\mathbf{r}_0$ at time t_0. Due to time translation invariance and space transition invariance (after averaging over disorder configurations), it is sufficient to consider the case $\mathbf{r}_0 = 0$ and $t_0 = 0$. Numerical results for the reduced probabilities $f_x(x, t) = \int \mathrm{d}y\, f(\mathbf{r}, t|\mathbf{r}_0, t_0)$ and $f_y(y, t) = \int \mathrm{d}x\, f(\mathbf{r}, t|\mathbf{r}_0, t_0)$ are shown in figure 7(a) and (b) for particles of energy $E = 0.3V_\mathrm{R}$ in a blue-detuned speckle potential. The distributions along the x- and y-directions present tails that can be well fitted by exponential functions. This behavior can be quantitatively related to the probability distribution of the sizes $\mathscr{L}$ of the allowed regions for a given energy E, which is exponentially small, $P_E(\mathscr{L}) \propto \exp(-a_E\mathscr{L}/\sigma_\mathrm{R})$ (see section 2.2 and figure 4). Consider particles trapped in lakes (allowed region) of linear length $\mathscr{L}$ along x. They chaotically explore the lakes and the linear density along x (averaged over the disorder) is almost uniform and scales as $1/\mathscr{L}$. Hence, the 'probability of diffusion' scales as $f_x(x, t \to \infty) \sim \int_x^\infty \mathrm{d}\mathscr{L}\ P_E(\mathscr{L})\frac{1}{\mathscr{L}}$. We then find that, for $x \gg \sigma_\mathrm{R}/a_E$, $f_x(x, t \to \infty)$ decays exponentially with the same characteristic length of $P_E(\mathscr{L})$, namely $\ln[f_x(x, t \to \infty)] \sim -a_E x/\sigma_\mathrm{R}$. For $E = 0.3V_\mathrm{R}$, we indeed find that, in the long-time and long distance limits, the decay rate of $f_x(x, t)$ ($b_x \simeq 0.11/\sigma_\mathrm{R}$; see figure 7(a)) is approximately the same as that of P_E ($a_E \simeq 0.12/\sigma_\mathrm{R}$; see the red triangles in figure 4(a)). The decay of $f_y(y, t)$ (see figure 7(b)) is simply related to that of $f_x(x, t)$ by taking into account the anisotropy factor $\lambda = \sigma_x/\sigma_y$ of the disorder. Therefore, the function $f_y(y, t)$ has exponential tails which decay λ times faster than $f_x(x, t)$.

3.4.2. Normal diffusion regime. For sufficiently long times and for energies above the percolation threshold, the dynamics is diffusive ($\alpha_r = 1$). This is shown in figures 1(e) and (f) where the solid lines are fits of $\langle r(t)^2\rangle = 2D_r(E/V_\mathrm{R}) \times t$ to the numerical data for $t \gg \tau^*$, with D_r as a fitting parameter (along the $r = x, y$ directions). We have studied the behavior of the diffusion coefficients $D_r(E/V_\mathrm{R})$ as a function of the particle energy, for blue- and red-detuned speckle potentials.

For a blue-detuned speckle potential, we find a clear power-law scaling of the diffusion coefficients versus the energy,

$$D_r(E/V_\mathrm{R}) = D_r^0 \times \left(\frac{E}{V_\mathrm{R}}\right)^{\gamma_r}, \quad V_\mathrm{R} > 0, \tag{15}$$

as evidenced by figure 8, which shows D_r versus E in the log–log scale. Fits of equation (15) to the numerical data, with D_r^0 and γ_r as fitting parameters, provide

$$D_x^0 \simeq (0.81\pm0.03)\ \sigma_\mathrm{R}^2/\tau_\mathrm{R}, \quad V_\mathrm{R} > 0, \tag{16a}$$

$$D_y^0 \simeq (0.26\pm0.01)\ \sigma_\mathrm{R}^2/\tau_\mathrm{R}, \tag{16b}$$

$$\gamma_x \simeq \gamma_y \simeq 3.15\pm0.04. \tag{16c}$$

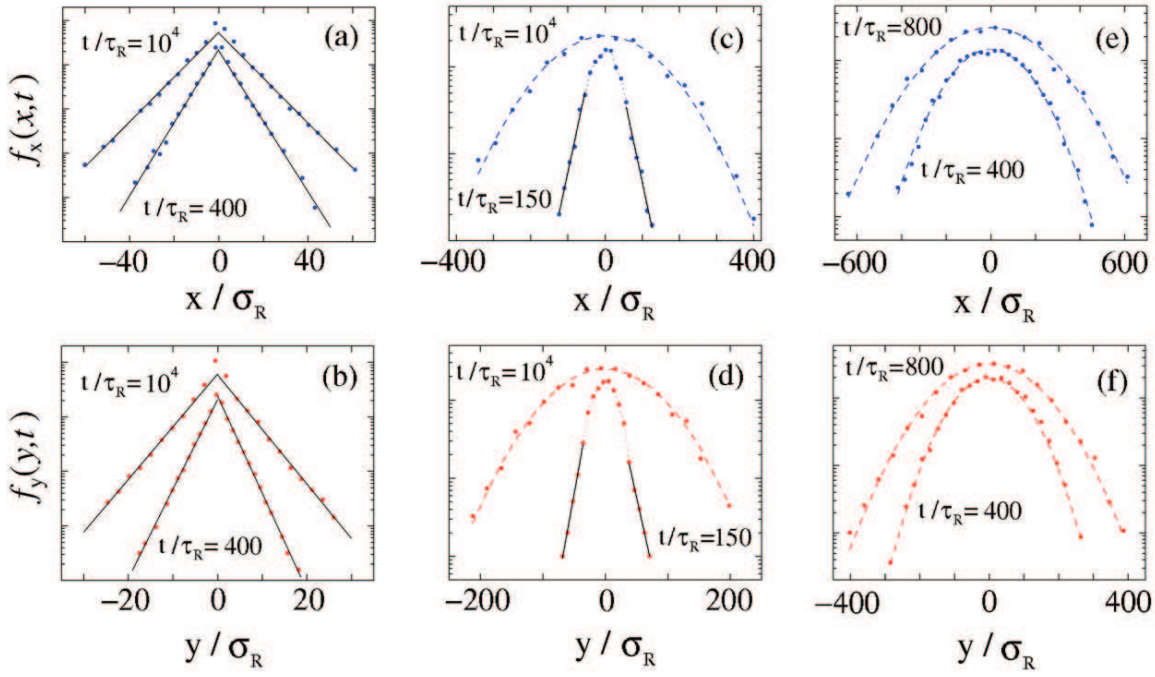

Figure 7. Integrated, average spatial distribution (dots) along the x- (upper row) and y- (lower row) directions in the semi-log scale. Different sets of data in each figure refer to different evolution times, vertically shifted for clarity and explicitly indicated. Here we consider a blue-detuned speckle potential. In panels (a) and (b) the energy is $E = 0.3V_R$. The solid lines are fits to the function $f_r(r, t) \approx e^{-b_r(t)|r|}$, which reproduces quite well the numerical results in the tails of the distributions. In particular, we have $b_x(t/\tau_R = 10^4) = 0.11/\sigma_R$ and $b_y(t/\tau_R = 10^4) = 0.22/\sigma_R$, the ratio between the two values being equal to the anisotropy factor $\lambda = 2$. In panels (c) and (d) the energy is $E = V_R$. The dotted lines are a guide to the eyes. The black lines are fits to exponential functions, $f(r, t) \approx e^{-b_r(t)|r|}$, for relatively short times ($t/\tau_R = 150$), while the dashed lines are $f(r, t) \approx e^{-r^2/4D_r(E)t}$, reproducing the data for long time periods. In panels (e) and (f), the energy is $E = 3V_R$ and the dashed lines are $f(r, t) \approx e^{-r^2/4D_r(E)t}$. The diffusion coefficients $D_r(E)$ are given by equations (15) and (16).

The diffusion coefficients D_r are characterized, within numerical error, by the same exponent γ along the x- and y-directions. In particular, the anisotropy of the diffusion does not depend much on the energy[9]. Interestingly, we find that, in the diffusion regime, the anisotropy factor of the diffusion, $D_x^0/D_y^0 \simeq 3.1$, significantly differs from the squared anisotropy factor of the disordered potential ($\lambda^2 = 4$). It shows that, in contrast to the classically localized regime, the anisotropy of the diffusion differs from the anisotropy of the disorder correlation function. This is further investigated in figure 9, which shows the ratio $(D_x/D_y)/\lambda^2$ as a function of $\lambda = \sigma_x/\sigma_y$ for $E = 3V_R$. For $\lambda > 1$, we find that $D_x(E)/D_y(E) < \lambda^2$.

[9] In the numerics, we find a slow dependence of the anisotropy factor of the diffusion, D_x/D_y, versus the energy E. However, in the whole energy window that is considered here, we find that $D_x/D_y \simeq 3.1$ with an accuracy better than 10%.

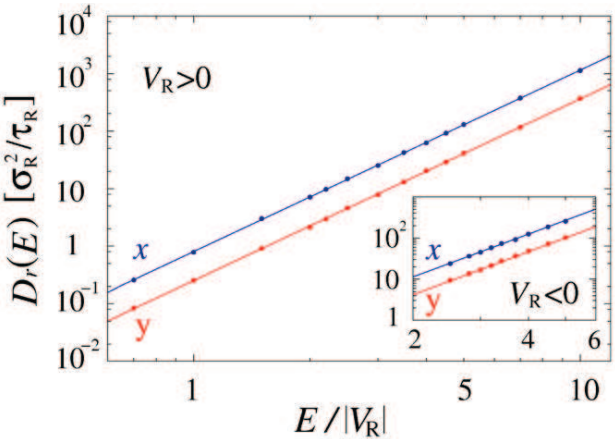

Figure 8. Diffusion coefficients $D_r(E)$ (dots; in units of σ_R^2/τ_R) along the $r = x, y$ directions. The results have been obtained numerically from fits of $\langle r(t)^2\rangle$, according to equation (13), for large times. The main figure shows the results for a blue-detuned speckle. Lines are the power-law fit to equation (15) and coefficients given by equation (16). The inset shows the diffusion coefficients $D_r(E)$ (dots) for a red-detuned speckle disorder, as a function of $E/|V_R|+2$. Lines are a power-law fit to equation (17) and coefficients given by equation (18). Numerical results have been obtained after averaging over 2000 realizations of the disordered potential.

For a red-detuned speckle potential, we have

$$D_r(E/V_R) = D_r^0 \times \left(\frac{E-2V_R}{|V_R|}\right)^{\gamma_r}, \quad V_R < 0. \tag{17}$$

Fits of equation (17) to the numerics with D_r^0 and γ_r as fitting parameters are shown in the inset of figure 8. We find that

$$D_x^0 \simeq (1.19 \pm 0.07)\ \sigma_R^2/\tau_R, \quad V_R < 0, \tag{18a}$$

$$D_y^0 \simeq (0.37 \pm 0.02)\ \sigma_R^2/\tau_R, \tag{18b}$$

$$\gamma_x \simeq \gamma_y \simeq 3.45 \pm 0.09. \tag{18c}$$

Compared to the blue-detuned case, we obtain significantly larger coefficients D_r^0 and larger exponents γ_r. However, the anisotropy factor is approximately unchanged, $D_x^0/D_y^0 \simeq 3.2$.

The power-law scaling of the diffusion coefficients versus the particle energy in large-energy windows is a rather general feature of particle diffusion problems [26, 29, 31]. Here, we find that, remarkably, the exponents $\gamma_{x,y}$ are almost the same along the two directions. For the energy window we are considering here, which is relevant to the experiment of [77], the disorder is strong. This is suggested by the fact that the diffusion coefficients at a given energy are significantly different for blue- and red-detuned speckle potentials. For higher energies, the theory of quantum diffusion shows that the diffusion coefficients, calculated in the Born approximation, only depend on the autocorrelation function of the disordered potential [69], which is the same for the blue- and red-detuned speckle potentials used in the present

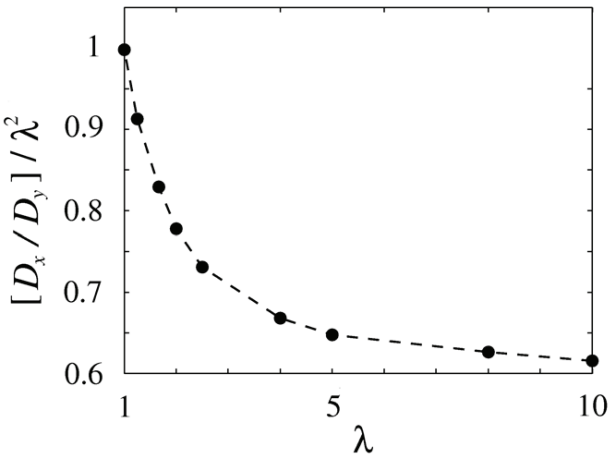

Figure 9. Anisotropy of the diffusion coefficient. The ratio $[D_x/D_y]/\lambda^2$ as a function of $\lambda = \sigma_x/\sigma_y$. Diffusion coefficients are obtained from the fit of $\langle r(t)^2\rangle$, according to equation (13) and for asymptotically large times. Dots are obtained for $E = 3V_R$ and by averaging over 2000 realizations of a blue-detuned speckle potential. The dashed lines are a guide to the eyes.

study (see section 2.1). For *isotropic* Gaussian correlation functions, one then finds that $\gamma = 2.5$ [31, 76]. Note, however, that the latter result holds for $E \gg V_R^2/E_R$, which can be equivalently written as $(E/V_R)^2 \gg (k\sigma_{x,y})^2$. The parameters used in the present work do not fulfill this condition since the validity of Newton's equation of motion requires that $k\sigma_{x,y} \gg 1$ and our calculations are run for $E \lesssim 10|V_R|$.

In the normal diffusion regime, we expect that the probabilities of diffusion are given by Gaussian functions [67]. In figures 7(e) and (f), we plot the (non-normalized) probability distributions along the x- and y-directions, taken at different times $t = 400\tau_R$ and $t = 800\tau_R$, for a blue-detuned speckle potential and for particles initially at the origin, $\mathbf{r}_0 = 0$. The numerical findings are in very good agreement with the functions $f_r(r, t) \propto e^{-r^2/4D_r(E)t}$, where the coefficients $D_r(E)$ are given by equations (15) and (16). We have checked that this holds for different energies in the normal diffusion regime.

Finally, we have studied the correlation functions $c_k(E, t) = \langle x^k(t)y^k(t)\rangle/\langle x^k(t)\rangle\langle y^k(t)\rangle$ for various integer values of k. For particles in the diffusion regime and for $t \gg \tau^*(E)$, we find that $c_k(E, t) \to 1$ for different values of k. This shows that, in the normal diffusion regime, the x- and y-variables are independent. Then, taking into account the results of figures 7(e) and (f), the probability of diffusion, i.e. the probability density to find a particle at the coordinate $\mathbf{r} = (x, y)$ at time t that was in $\mathbf{r}_0 = (x_0, y_0)$ at time t_0, is given by

$$f_E(\mathbf{r}, t|\mathbf{r}_0, t_0) = \frac{e^{-\frac{(x-x_0)^2}{4D_x(E)(t-t_0)}}}{\sqrt{4\pi D_x(E)}} \frac{e^{-\frac{(y-y_0)^2}{4D_y(E)(t-t_0)}}}{\sqrt{4\pi D_y(E)}} \frac{\Theta(t-t_0)}{(t-t_0)}. \tag{19}$$

3.4.3. Sub-diffusion regime. Anomalous diffusion occurs in a variety of physical systems [67, 86, 90] and has been experimentally studied in [64, 91–93] for instance. It is defined by the condition $\alpha_r \neq 1$ in equation (13) and two physically different regimes should be

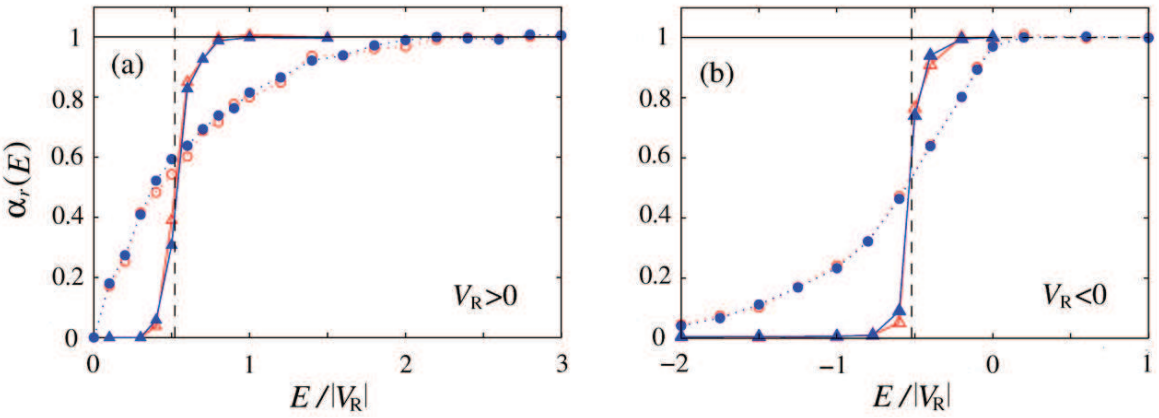

Figure 10. Scaling coefficient $\alpha_r(E)$ obtained from a fit of $\langle r(t)^2\rangle$ (according to equation (13)) at intermediate times, $100 \lesssim t/\tau_R \lesssim 1000$ (circles), and at larger times, $t/\tau_R \gtrsim 1000$ (triangles). The fits are shown, for instance, in figures 1(d)–(f). Solid and dotted lines are a guide to the eyes. Different colors refer to the $r = x$ (blue lines and filled symbols) and $r = y$ (red lines and empty symbols) directions. Panels (a) and (b) refer to blue- and red-detuned speckle potentials, respectively. In each panel, the vertical dashed black line is the percolation threshold, $E_c = 0.52V_R$.

distinguished: sub-diffusion when $0 < \alpha_r < 1$ and super-diffusion when $1 < \alpha_r < 2$. In our case, super-diffusion only shows up for $t \sim \tau^*$ in the crossover from ballistic expansion ($\alpha_r = 2$ for $t \lesssim \tau^*$) to normal diffusion or sub-diffusion (for $t \gtrsim \tau^*$). Sub-diffusion is more relevant to our study. For a blue-detuned speckle potential, transient sub-diffusive behavior is found for $E \lesssim 2V_R$ and long (although not asymptotic) time scales with $t \gg \tau^*$. For instance, the fits of equation (13) to $\langle r(t)^2\rangle$ in figures 1(d) and (e), at intermediate times and with $\tilde{D}_r$ and α_r as fitting parameters, (dashed lines) give $\alpha_r < 1$. The scaling coefficients α_r, as obtained from such fits in two different time windows, are plotted as a function of energy in figure 10 for blue-detuned (left panel) and red-detuned (right panel) speckle potentials. The value of α_r obtained from the fits in an intermediate time window ($10^2\tau_R < t < 10^3\tau_R$) smoothly crosses over from $\alpha_r = 0$ to $\alpha_r = 1$ when crossing the percolation threshold E_c. For very long time periods ($t > 10^3\tau_R$), the crossover is very sharp, which is compatible with an abrupt transition between two asymptotically relevant dynamical regimes: below the percolation threshold ($E < E_c$), the mean square displacement $\langle r(t)^2\rangle$ evolves from sub-diffusion to classical localization (see figure 1(e)). Conversely, slightly above the percolation threshold ($E \gtrsim E_c$), $\langle r(t)^2\rangle$ evolves from sub-diffusion to normal diffusion (see figure 1(f)). Notably, this case shows that the sub-diffusion regime cannot always be considered a precursor of localization.

While the sub-diffusive behavior is not asymptotic, it is however experimentally relevant. In fact, sub-diffusion is observed for $E \sim V_R$, at times of the order of $\sim 200\tau_R$, which corresponds to ~ 100 ms for the parameters of [77], which is the typical time scale of the experiment. In the sub-diffusion regime, the probability density $f(\mathbf{r}, t|\mathbf{r}_0, t_0)$ is characterized by exponentially decaying tails (see figures 7(a)–(d)). We interpret this result by analogy with the behavior described above in the classical localization regime. Slightly above the percolation threshold, there exist allowed regions of finite size that are disconnected from each other or

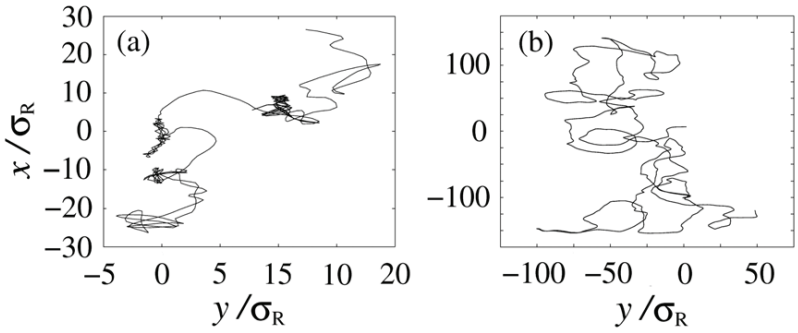

Figure 11. Trajectory of a particle of energy E in an anisotropic, blue-detuned speckle potential, obtained by solving equations (8). In panel (a) the energy is $E = V_R$ and the trajectory is characterized by relatively small regions where the particle spends long time periods. This behavior gives rise to transient sub-diffusion. Panel (b) shows the trajectory for a particle of energy $E = 3V_R$. The dynamics is diffusive and qualitatively similar to Brownian motion [67].

connected by very thin bottlenecks to a percolating cluster. Then, as illustrated in figure 11(a), a particle stays for long time periods in the same lake where it behaves similarly to below the percolation threshold. In particular, its dynamics is sub-diffusive. As discussed above, this persists for asymptotically large times when classical localization occurs (for $E \leqslant E_c$; figures 7(a) and (b)). Above the percolation threshold ($E > E_c$) however, the particle can find a path connecting the lake to another one after a sufficiently long exploration of the lake. It then spends a long time in the new lake before switching to another one and so on[10]. For a longer time scale and larger space scale, the dynamics results from random jumps of the particle from a trapping region to another one, hence developing normal diffusion, similarly to usual Brownian motion. In particular, the probability of diffusion becomes Gaussian (see figures 7(c) and (d) for a sufficiently long time). Here, the existence of long waiting times would explain the transient sub-diffusive regime obtained at intermediate times. Note that for higher energies, where no transient sub-diffusion is found, the trajectory of a particle does not show long waiting times and reminds one of Brownian motion even on a short time scale (see figure 11(b)).

4. Expansion of an atomic cloud

Section 3 presents a detailed analysis of the transport regimes for particles with a fixed energy. In typical experiments with cold atoms, transport is investigated from the behavior of a cloud of atoms with a broad energy distribution. In this section, we study the expansion of an atomic gas by considering the atoms as non-interacting classical particles moving in a 2D disordered potential. We take into account the energy distribution of the gas and discuss our findings in the light of the results of section 3.

[10] Similar behavior was identified in dissipative, periodic optical lattices [94]. In the latter case, escape from trapping regions was induced by dissipative effects. In the present case, the potential is purely conservative and escape from (nearly) trapping regions is due to the topography of the potential near the percolation threshold, which shows thin connecting paths.

4.1. Energy distribution of an initially trapped gas

The aim of this subsection is to calculate the energy distribution of a thermal gas of non-interacting particles initially trapped. We will consider two experimentally relevant cases in which the disorder is initially combined with the trap or switched on after releasing the trap. The energy distribution is highly sensitive to the way the disorder is turned on.

Quite generally, in transport experiments with cold atoms, the atomic cloud is initially in equilibrium in a trap described by the potential $V_0(\mathbf{r})$. The initial single-particle classical Hamiltonian is $H_0(\mathbf{r}, \mathbf{p}) = |\mathbf{p}|^2/2m + V_0(\mathbf{r})$ and the phase-space density distribution for a thermal gas at temperature T reads

$$\rho_0(\mathbf{r}, \mathbf{p}) = \frac{\mathrm{e}^{-\beta H_0(\mathbf{r},\mathbf{p})}}{Z_0}, \tag{20}$$

where $Z_0 = \int \mathrm{d}\mathbf{r}'\mathrm{d}\mathbf{p}'\, \mathrm{e}^{-\beta H_0(\mathbf{r}',\mathbf{p}')}$, $\beta = 1/k_\mathrm{B}T$ and k_B is the Boltzmann constant. At time $t = 0$, the confinement is switched off and the non-interacting gas expands in the disordered potential $V(\mathbf{r})$. The dynamics is then governed by the single-particle Hamiltonian $H(\mathbf{r}, \mathbf{p}) = |\mathbf{p}|^2/2m + V(\mathbf{r})$ and the joint distribution of energy and position at time $t = 0^+$ is

$$n(\mathbf{r}, E) = \int \mathrm{d}\mathbf{p}\, \rho_0(\mathbf{r}, \mathbf{p})\, \delta(E - H(\mathbf{r}, \mathbf{p})) \tag{21}$$

$$= \frac{\beta\, \mathrm{e}^{-\beta(E-V(\mathbf{r})+V_0(\mathbf{r}))}}{\int \mathrm{d}\mathbf{r}'\, \mathrm{e}^{-\beta V_0(\mathbf{r}')}} \Theta(E - V(\mathbf{r})). \tag{22}$$

In the following, we calculate the disorder-averaged energy distribution $\langle n(\mathbf{r}, E)\rangle$, distinguishing two experimentally relevant situations: (i) the gas is prepared in a bare trap, so that $V_0(\mathbf{r}) = V_\mathrm{trap}(\mathbf{r})$, where $V_\mathrm{trap}(\mathbf{r})$ is the potential of the trap, which is independent of the disordered potential. The disorder is suddenly switched on after the gas has thermalized in the trap. (ii) The gas is prepared in the trap and in the presence of disorder, so that $V_0(\mathbf{r}) = V_\mathrm{trap}(\mathbf{r}) + V(\mathbf{r})$, which now depends on the disordered potential.

Case (i). If $V_0(\mathbf{r})$ does not depend on the disordered potential, averaging the distribution equation (22) gives

$$\langle n(\mathbf{r}, E)\rangle = \frac{\beta\, \mathrm{e}^{-\beta V_0(\mathbf{r})}}{\int \mathrm{d}\mathbf{r}'\, \mathrm{e}^{-\beta V_0(\mathbf{r}')}} \int_{-\infty}^{E} \mathrm{d}V\, P(V)\, \mathrm{e}^{-\beta(E-V)},$$

where $P(V)$ is the one-point probability distribution of the disordered potential. It is interesting to note that, in a homogeneous disorder and independent of the specific form of the initial trapping potential, the energy and position variables decouple:

$$\langle n(\mathbf{r}, E)\rangle = n_\mathrm{trap}(\mathbf{r})\langle n(E)\rangle, \tag{23}$$

where

$$n_\mathrm{trap}(\mathbf{r}) = \int \mathrm{d}\mathbf{p}\, \rho_0(\mathbf{r}, \mathbf{p}) = \frac{\mathrm{e}^{-\beta V_0(\mathbf{r})}}{\int \mathrm{d}\mathbf{r}'\mathrm{e}^{-\beta V_0(\mathbf{r}')}} \tag{24}$$

is the initial spatial distribution and

$$\langle n(E)\rangle = \beta \int_{-\infty}^{E} \mathrm{d}V\, P(V)\mathrm{e}^{-\beta(E-V)} \tag{25}$$

is the average energy distribution in the presence of disorder. For a speckle potential, equation (2) holds and the integral in equation (25) can be easily done. In particular, for a blue-detuned speckle potential, we find that[11]

$$\langle n(E)\rangle = \frac{\beta}{1-\beta V_{\mathrm{R}}}[\mathrm{e}^{-\beta E} - \mathrm{e}^{-E/V_{\mathrm{R}}}]\,\Theta(E). \tag{26}$$

A plot of equation (26) as a function of energy is shown in figure 12(a)[12] for different values of βV_{R}.

Case (*ii*). If, in contrast, $V_0(\mathbf{r})$ depends on the disordered potential, the calculation of equation (22) is difficult since both the numerator and the denominator depend on the specific disorder configuration. A simplified expression is obtained if the thermal gas extends, in the initial trapping potential $V_0(\mathbf{r})$, over a region much larger than the correlation length of the disorder. This condition can be fulfilled for a sufficiently shallow confining trap. In this case, the self-averaging properties of the disordered potential allow us to substitute the integral $\int \mathrm{d}\mathbf{r}'\,\mathrm{e}^{-\beta V_0(\mathbf{r}')}$ by the disorder-averaged value $\langle \int \mathrm{d}\mathbf{r}'\,\mathrm{e}^{-\beta V_0(\mathbf{r}')}\rangle = \int \mathrm{d}\mathbf{r}'\mathrm{e}^{-\beta V_T(\mathbf{r}')} \int \mathrm{d}V\,P(V)\mathrm{e}^{-\beta V}$. We thus find that, also in this case, the energy and position variables decouple. Then, equation (23) still holds, with the same density distribution as given by equation (24), but with a different energy distribution,

$$\langle n(E)\rangle = \frac{\beta\,\mathrm{e}^{-\beta E}\int_{-\infty}^{E}\mathrm{d}V\,P(V)}{\int_{-\infty}^{+\infty}\mathrm{d}V\,P(V)\mathrm{e}^{-\beta V}}. \tag{29}$$

In particular, for a blue-detuned speckle potential, we have (see footnote 10)

$$\langle n(E)\rangle = \beta(1+\beta V_{\mathrm{R}})\mathrm{e}^{-\beta E}\left[1-\mathrm{e}^{-E/V_{\mathrm{R}}}\right]\Theta(E). \tag{30}$$

In the case of an isotropic harmonic trap $V_{\mathrm{trap}}(\mathbf{r}) = m\omega^2|\mathbf{r}|^2/2$, we find that $n_{\mathrm{trap}}(\mathbf{r}) = \mathrm{e}^{-|\mathbf{r}|^2/2{\sigma_T}^2}/2\pi\sigma_T^2$, where $\sigma_T = \sqrt{k_{\mathrm{B}}T/m\omega^2}$. The self-averaging condition invoked above is thus

[11] For a red-detuned speckle potential ($V_{\mathrm{R}} < 0$), equation (25) is given by

$$\langle n(E)\rangle = \frac{\beta}{1+\beta|V_{\mathrm{R}}|}\begin{cases}\mathrm{e}^{+E/|V_{\mathrm{R}}|}, & \text{for } E\leqslant 0,\\ \mathrm{e}^{-\beta E}, & \text{for } E\geqslant 0,\end{cases}$$

while equation (29) is

$$\langle n(E)\rangle = \beta(1-\beta|V_{\mathrm{R}}|)\begin{cases}\mathrm{e}^{-E(\beta-1/|V_{\mathrm{R}}|)}, & \text{for } E\leqslant 0,\\ \mathrm{e}^{-\beta E}, & \text{for } E\geqslant 0.\end{cases}$$

[12] Explicit calculations give

$$n_<(E) = 1 - \frac{\mathrm{e}^{-\beta E} - \beta V_{\mathrm{R}}\,\mathrm{e}^{-E/V_{\mathrm{R}}}}{1-\beta V_{\mathrm{R}}} \tag{27}$$

for the distribution equation (26) and

$$n_<(E) = 1 - \mathrm{e}^{-\beta E}[1+\beta V_{\mathrm{R}}(1-\mathrm{e}^{-E/V_{\mathrm{R}}})] \tag{28}$$

for the distribution equation (30). They correspond to a thermal gas in equilibrium in a bare and a disordered trap, respectively. In the high temperature limit, $\beta V_{\mathrm{R}} \to 0$, equations (27) and (28) tend to $n_<(E) \approx (\mathrm{e}^{-E/V_{\mathrm{R}}} + E/V_{\mathrm{R}} - 1)\beta V_{\mathrm{R}} + o(\beta V_{\mathrm{R}})^2$. In the low temperature limit, $\beta V_{\mathrm{R}} \to \infty$, equation (27) tends to $n_<(E) \approx 1 - \mathrm{e}^{-E/V_{\mathrm{R}}}$ while equation (28) tends to $n_<(E) = 1$.

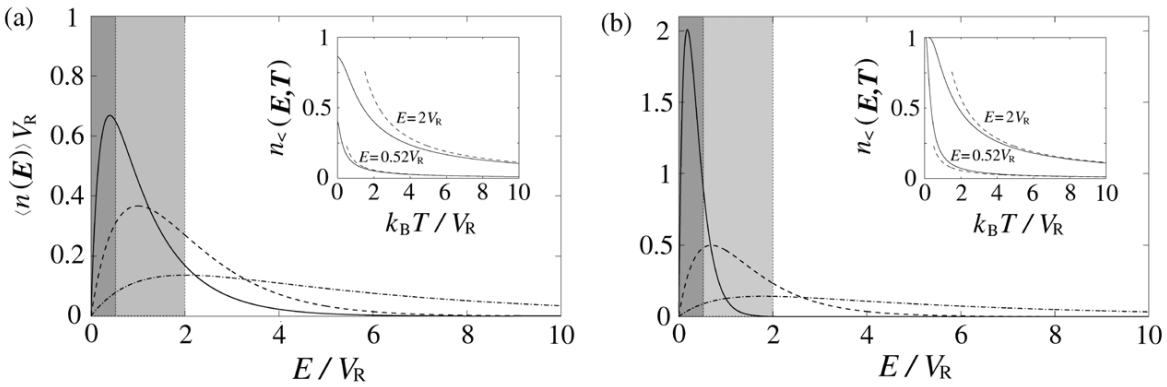

Figure 12. Disorder-averaged energy distributions of the atomic cloud. Panel (a) is equation (26), obtained when the speckle potential is suddenly switched on after releasing the trap where the atomic cloud is initially in equilibrium (case (i)). Panel (b) is equation (30) and corresponds to a thermal cloud in equilibrium in a disordered trap (case (ii)). The different curves refer to different values of V_R: $V_R = 5\,k_BT$ (solid line), $V_R = k_BT$ (dashed line) and $V_R = 0.2\,k_BT$ (dot-dashed line). The gray-shaded region indicates sub-diffusive particles ($E \leqslant 2\,V_R$) and the darkest region classically localized particles ($E \leqslant 0.52\,V_R$; see section 3). Inset: density of particles with energy smaller than E (solid lines). The dashed lines are a prediction in the large temperature limit $k_BT \gg V_R$ (see footnote 11).

$\sigma_T \gg \sigma_R$. A plot of equation (30) as a function of energy is shown in figure 12(b) for different values of βV_R. Equations (26) and (30) tend, in the high-temperature limit ($k_BT \gg E$, V_R), to $\langle n(E)\rangle = \beta(1 - e^{-E/V_R})$. At low temperature ($k_BT \ll V_R$), the two distributions differ substantially, equation (30) being more strongly peaked at small energies.

The insets of figure 12 show the fraction of particles with energy lower than E, $n_<(E, T) \equiv \int_0^E d\epsilon\, \langle n(\epsilon)\rangle$ (see footnote 11), as a function of temperature and for various energies. In particular, it shows the fraction of atoms in the classically localized regime, $n_<(E = 0.52V_R, T)$, and below the transient sub-diffusive regime threshold, $n_<(E = 2V_R, T)$, identified in section 3. The dotted line is the asymptotic behavior for large temperatures, $n_<(E, T) = (e^{-E/V_R} + E/V_R - 1)\beta V_R$, which is the same for both cases (i) and (ii). When the gas thermalizes in the trap and in the presence of disorder (case (ii) described by equation (30)), the fraction of particles at low energy is larger than that in the case when the disorder is suddenly ramped after releasing the confining trap (case (i) described by equation (26)). In case (ii), all particles can be classically localized at low temperature (i.e. $n_<(E = 0.52V_R, T) \to 1$ when $T \to 0$). Conversely, in case (i), the speckle potential is switched on after releasing the initial confining trap, which transfers an average energy $\sim V_R$ to all particles and the fraction of particles at low energy is depleted.

4.2. Expansion of the atomic gas

We now study the dynamics of an atomic cloud initially trapped in a pure harmonic potential (i.e. without disorder, case (i)). At $t = 0$ the trap is released and the atoms expand in a blue-detuned speckle potential. As shown above, the energy and the initial position of the atoms are uncorrelated variables when averaging over disorder configurations. In our simulations, the

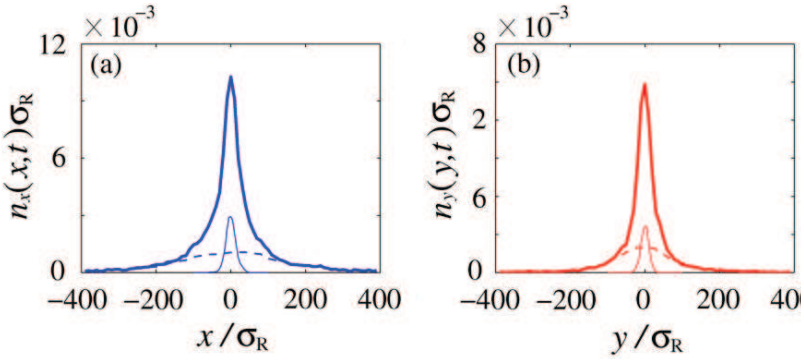

Figure 13. Integrated spatial density distribution of an expanding thermal gas in a 2D disordered potential. The thick solid line is the integrated spatial density distribution (a) $n_x(x,t) \equiv \int \mathrm{d}y\, n(\mathbf{r},t)$ and (b) $n_y(y,t) \equiv \int \mathrm{d}x\, n(\mathbf{r},t)$, where $n(\mathbf{r},t)$ is given by equation (31). Here, $V_\mathrm{R} = k_\mathrm{B}T$, $t = 400\tau_\mathrm{R}$, the initial distribution is a Gaussian of width $\sigma_T = 10\sigma_\mathrm{R}$ and the energy distribution is given by equation (26). In the numerical simulation, we used 100 00 particles. We also plot the contributions of particles with energy $E > 2V_\mathrm{R}$ (dashed line) and with energy $E \leqslant 0.52V_\mathrm{R}$ (thin solid line). Note that for the time considered here, the transient sub-diffusive regime is relevant and the fraction of atoms in this regime cannot be neglected.

energy is randomly chosen according to equation (26), while the initial position is randomly chosen according to a Gaussian distribution of width $\sigma_T = 10\sigma_\mathrm{R}$, which is relevant to typical experiments [77]. We expect this approach to be reproducible *in a single run of the experiment* since, for $\sigma_T \gg \sigma_\mathrm{R}$, the speckle disorder 'self-averages' over the atomic cloud.

Density distribution. An important feature of the experiments with cold atoms is the possibility of obtaining an image of the density cloud at different expansion times. For instance, it has been crucial in the recent observation of Anderson localization with Bose–Einstein condensates in the quasi-1D geometry [61, 62].

The time-dependent density profile (averaged over different realizations of the disordered potential) is calculated by integrating the probability of diffusion over all energies and all initial positions

$$n(\mathbf{r},t) = \int \mathrm{d}\mathbf{r}_0 \int \mathrm{d}E\, n_\mathrm{trap}(\mathbf{r}_0)\, \langle n(E)\rangle\, f_E(\mathbf{r},t|\mathbf{r}_0,0), \tag{31}$$

where $n_\mathrm{trap}(\mathbf{r}_0)$ is the spatial density distribution in the initial trap. As noted in the previous paragraph, for a thermal gas, the initial joint position–energy distribution decouples into the product of separate distributions. This feature is particular to the case of an initial thermal distribution. For instance, it does not hold for initially expanding Bose–Einstein condensates as considered in [31, 35, 75]. The quantity $f_E(\mathbf{r},t|\mathbf{r}_0,0)$ gives the probability distribution to find a particle of energy E at position $\mathbf{r}$ and at time $t \geqslant 0$, assuming that it was in $\mathbf{r}_0$ at time $t = 0$. Its behavior has been discussed in section 3 for particles of fixed energy in various transport regimes. The integrated density profiles at time $t = 400\tau_\mathrm{R}$ are shown as thick solid lines in figure 13. It is striking that these profiles are, in general, not Gaussian. They present a pronounced central peak, which is partially due to the contributions of the atoms in the

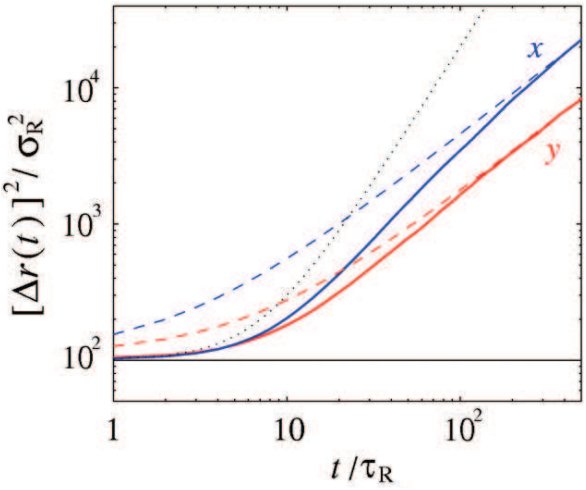

Figure 14. Mean square size, $[\Delta r(t)]^2$, as a function of time, in the $r = x$ (solid blue line) and $r = y$ (solid red line) directions. The dotted line is equation (32) and has been obtained by assuming a ballistic expansion for all atoms. The dashed lines are equation (33), corresponding to all particles behaving diffusively. The horizontal line is the mean square size of the initial cloud, given by σ_T^2. Here $V_R = k_B T$ and $\sigma_T = 10\sigma_R$.

classical localization and sub-diffusive regimes. It is worth stressing that, even taking into account only the fraction of atoms in the diffusive regime, for which the probability of diffusion, $f_E(\mathbf{r}, t|\mathbf{r}_0, 0)$, is a Gaussian function (see equation (19)), the overall distribution is, in general, not Gaussian. This is due to the integration over the energy variable in equation (31) and to the strong energy dependence of the diffusion coefficients [75, 76]. In fact, since the particles in the diffusive regime determine the long tails of $n(\mathbf{r}, t)$, the spatial distribution can be used to extract the diffusion coefficients from experimental data (see [77] and section 5).

Root mean square size. A simple quantity that can be extracted from the density profiles is the root mean square (rms) size of the atomic cloud, $\Delta r(t) \equiv \sqrt{\int d\mathbf{r}\, r^2\, n(\mathbf{r}, t)}$, in the $r = x, y$ direction and where $n(\mathbf{r}, t)$ is given by equation (26). The evolution of the rms sizes in the two directions is shown in figure 14, for $V_R = k_B T$. At sufficiently short time periods, $t \ll \tau^*(\bar{E})$, where $\bar{E}$ is the typical energy of the atomic cloud[13], the rms size can be obtained by assuming that all the atoms behave ballistically[14]. In this case, we find that

$$[\Delta r(t)]^2 = \sigma_T^2 + \frac{1 + \beta V_R}{\beta V_R}\sigma_R^2 \left(\frac{t}{\tau_R}\right)^2, \tag{32}$$

where $\sigma_T = \sqrt{k_B T/m\omega^2}$ is the rms size of the initial atomic cloud. Equation (32) is shown by the dotted black line in figure 14. For long time periods, $t \gg \tau^*(\bar{E})$, the rms size of the atomic cloud can be calculated by assuming that all the particles behave diffusively. This approximation

[13] For the distribution of equation (26), we have $\bar{E} = k_B T + V_R$. For the parameters of figure 14, $k_B T = V_R$, we have $\bar{E} = 2V_R$ and $\tau^*(\bar{E})/\tau_R \sim 10$.

[14] For an isotropic, ballistic expansion we have $f_E(\mathbf{r}, t; \mathbf{r}_0, t_0) = \Theta(t - t_0)\,\delta[|\mathbf{r} - \mathbf{r}_0| - (t - t_0)\sqrt{2E/m}]/2\pi(t - t_0)\sqrt{2E/m}$.

is legitimate in the long-time limit if the fraction of classically localized particles is negligible, which strongly depends on the ratio $k_B T/V_R$. In this case, the evaluation of equation (31) using equations (26), (19) and (15) gives

$$[\Delta r(t)]^2 \simeq 2D_r^0 \sigma_R^2 \frac{[1-(\beta V_R)^{\gamma_r+1}]\Gamma(\gamma_r+1)}{(1-\beta V_R)(\beta V_R)^{\gamma_r}} \frac{t}{\tau_R}, \tag{33}$$

where $\Gamma(x)$ is the Gamma function. In figure 14, we show equation (33) calculated for the parameters D_r^0 and γ_r given by equations (16). We find good agreement with the numerical findings for long time periods, despite the fact that the fraction of localized or sub-diffusive atoms is $n_<(E=2V_R, T) \simeq 70\%$. Hence, equation (33) could be used experimentally to extract the values of γ_r and D_r^0 characterizing the diffusive regime and thus verify the results of section 3.4.

5. Experimental results

The study of classical transport of cold gases in a 2D disordered potential is experimentally feasible. A 2D disordered potential can be created experimentally by a speckle field, as discussed in section 2.1. The atoms can be confined to a plane by a tight transversal harmonic trap of frequency ω_z. The dynamics in the transverse direction can be neglected if $k_B T$ is much smaller than the vertical confinement energy $\hbar\omega_z$.

In recent experiments [77], we have studied the dynamics of a cloud of ^{87}Rb atoms in a speckle disorder. The geometry is not strictly 2D since $k_B T \approx k_B \times 200(20)\,\mathrm{nK} \approx 6\hbar\omega_z$, where $\omega_z/2\pi = 680\,\mathrm{Hz}$. Therefore, taking into account the harmonic confinement, the external potential is given by $V(x, y, z) + m\omega^2 z^2/2$, with $V(x, y, z) = V_{\mathrm{iso}}(x\sin\theta - z\cos\theta, y)$, where $V_{\mathrm{iso}}(u, v)$ is a 2D isotropic blue-detuned speckle potential with correlation length $\sigma = 0.8\,\mu\mathrm{m}$ and Gaussian autocorrelation function. In the experiment, the speckle disorder is tilted by $\theta = 30^\circ$ with respect to the horizontal plane. This makes the disorder anisotropic in the expansion plane, with correlation lengths $\sigma_x = 1.6\,\mu\mathrm{m}$ and $\sigma_y = 0.8\,\mu\mathrm{m}$, and anisotropy factor $\lambda = \sigma_x/\sigma_y = 2$. The speckle is assumed to be invariant along its propagation axis. This is a reasonable approximation since the longitudinal correlation length, $\sigma_{\mathrm{long}} = 9\,\mu\mathrm{m}$, is large compared with the vertical size of the cloud, $(k_B T/m\omega_z^2)^{1/2} \approx 1\,\mu\mathrm{m}$.

Using a classical particle model is a reasonable approximation since $k\sigma_x \approx 10$ and $k\sigma_y \approx 5$, where $k = \sqrt{mk_B T}/\hbar$. In addition, the 'correlation energy' $E_R = \hbar^2/m\sigma_R \approx k_B \times 2\,\mathrm{nK}$ is typically more than one order of magnitude smaller than the amplitude of the disorder $V_R = k_B \times 53\,\mathrm{nK}$. Within these conditions, the localization length should be much larger than the system size ($\sim 1\,\mathrm{mm}$ in each direction) and one can expect that quantum interference effects can be neglected. Due to the tilting angle of the speckle pattern, which couples the in-plane dynamics to the dynamics in the confined direction, the system is 3D rather than purely 2D. Therefore, the classical equations of motions (8) must be adapted to take into account the vertical confinement[15].

[15] In the 3D case, the classical equations of motion read

$$\frac{d\tilde{\mathbf{r}}}{d\tilde{t}} = \tilde{\mathbf{p}},$$

$$\frac{d\tilde{\mathbf{p}}}{d\tilde{t}} = -\tilde{\nabla}\left[v_{\mathrm{iso}}(\tilde{x}\sin\theta - \tilde{z}\cos\theta, \tilde{y}) + \frac{(\omega_z\tau_R)^2\tilde{z}^2}{2}\right],$$

where the reduced variables are defined in section 3.1.

Remarkably, the results of this 3D model differ only slightly from the results presented above for the purely 2D situation. The two asymptotic regimes (classical localization and normal diffusion) are unchanged since the 3D potential results from a cylindrical stretching of a 2D potential. We also find a transient sub-diffusion regime in approximately the same energy window and time scale as for the pure 2D case, $0.52V_R \lesssim E \lesssim 2V_R$. For each regime, the dynamics is qualitatively similar for both the pure 2D and the trapped 3D cases. The diffusion coefficients have a power-law scaling analogous to equation (15) [77]. The numerical simulations give diffusion parameters slightly different from the ones of equation (16):

$$D_x^0 = (1.20 \pm 0.05)\ \sigma_R^2/\tau_R, \tag{34a}$$

$$D_y^0 = (0.33 \pm 0.02)\ \sigma_R^2/\tau_R, \tag{34b}$$

$$\gamma_x \simeq \gamma_y = 2.8 \pm 0.06. \tag{34c}$$

For the parameters of the experiment, $V_R = k_B \times 53\,\mathrm{nK}$, $\sigma_R = \sigma_x = 1.6\,\mu\mathrm{m}$ and $\tau_R = 0.71\,\mathrm{ms}$, we obtain $D_x^0 = 4.3\,\mu\mathrm{m}^2\,\mathrm{ms}^{-1}$ and $D_y^0 = 1.2\,\mu\mathrm{m}^2\,\mathrm{ms}^{-1}$.

In the experiment, the speckle disorder is switched on after releasing the initial confining trap in the (x, y) direction, while the transverse confinement is kept during the whole expansion. We expect that a few collisions redistribute the energy between the atoms during the first 10 ms of the expansion. The calculation of $\langle n(E)\rangle$ is modified compared to equation (30) in order to include the contribution of the different vertical energy levels. Taking into account the quantization of the transverse harmonic oscillator, we obtain

$$\langle n(E)\rangle \propto \mathrm{e}^{-E/k_BT} \sum_{n=0}^{E/\hbar\omega_z} \left(1 - \mathrm{e}^{(n\hbar\omega_z - E)/V_R}\right), \tag{35}$$

which is plotted in figure 15. For the considered experimental parameters, the fraction of classically localized atoms is about 0.4% of the total number of atoms, while the fraction of subdiffusive atoms for the time scale of the experiment is about 6%.

The goal of the experiment is to extract the energy-dependent diffusion coefficients in the 2D anisotropic speckle potential. They are experimentally measured by analyzing the complete 2D column density profile, obtained experimentally by fluorescence imaging along the vertical axis (see figure 16). In order to fit the experimental density, we use equations (19) (with $t_0 = 0$) and (31) convolved by a Gaussian function that takes into account the resolution of the imaging system. Using the fact that, for an initial harmonic trap, $n_{\mathrm{trap}}(\mathbf{r}_0)$ is a Gaussian function, we find that

$$n(x, y, t) = \int \mathrm{d}E\ \langle n(E)\rangle \frac{\mathrm{e}^{-\frac{x^2}{2(2D_x(E)t+\sigma_0^2)}}\,\mathrm{e}^{-\frac{y^2}{2(2D_y(E)t+\sigma_0^2)}}}{2\pi\, t\,\sqrt{(2D_x(E)t+\sigma_0^2)(2D_y(E)t+\sigma_0^2)}}, \tag{36}$$

where $\langle n(E)\rangle$ is given by equation (35) and $\sigma_0 = 15\,\mu\mathrm{m}$ as determined experimentally. Equation (36) assumes that all the particles behave diffusively. This is a good approximation since, for the experimental parameters, the fraction of classically localized and sub-diffusive particles is small. Diffusion coefficients are extracted by using the power-law scaling predicted numerically, $D_r(E) = D_r^0 \times (E/V_R)^{\gamma_r}$ $(r = x, y)$. Figure 16 shows that the 2D density distribution is well reproduced by the fitting function, equation (36), with D_r^0 and γ_r as fitting

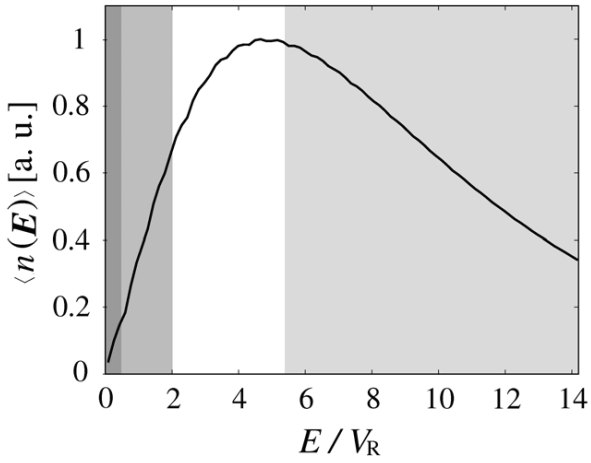

Figure 15. Disorder-averaged energy distribution in the experiments of [77]. The solid line is equation (35). Gray regions indicate different dynamical regimes: classical localization for $E < 0.52V_R$ (darkest region), transient sub-diffusion for $E < 2V_R$ (gray region), diffusion for $2V_R < E < 5.5V_R$ (white region) and transient ballistic expansion (see text for details) for $E > 5.5V_R$ (light gray region). Here the amplitude of the disordered potential is $V_R = k_B \times 53\,\mathrm{nK}$ and the temperature $T = 220\,\mathrm{nK}$.

parameters. Experimentally, we find that

$$D_x^0 = 5.5 \pm 2.7\,\mu\mathrm{m}^2\,\mathrm{ms}^{-1}, \tag{37a}$$

$$D_y^0 = 1.6 \pm 0.8\,\mu\mathrm{m}^2\,\mathrm{ms}^{-1}, \tag{37b}$$

$$\gamma_x \simeq \gamma_y = 3.3 \pm 0.3. \tag{37c}$$

These values are, within experimental errors, in fair agreement with the classical theory (see equations (34) and the text below them). In particular, the algebraic scaling inferred from the numerical simulations is consistent with the experimental findings. In addition, these results show the possibility of extracting the single-particle diffusion coefficients from the dynamics of an atomic cloud.

We finally note that the high-energy atoms are ballistic on the time scale of the experiment (see figure 15). The crossover between the ballistic and the diffusive behavior takes place when the Boltzmann time τ_B ($= 4D(E)/v^2$, where $v = \sqrt{E/m}$ is the rms in-plane velocity) is of the order of the expansion time $t = 200\,\mathrm{ms}$. The same crossover between ballistic and diffusive behavior is seen as a function of time in figure 1(c) for a given energy. For the experimental parameters, we estimate that below $E_{\text{bal-dif}} \approx 5.5V_R$, the atoms are diffusive (calculated in the x-direction, which gives the lower estimate of $E_{\text{bal-dif}}$). Above this value, the atoms may be ballistic on the time scale of the experiment. In this case, they however extend over a distance $vt \gtrsim 1\,\mathrm{mm}$, larger than the spatial size used in figure 16 where we fit our diffusive distribution. Ballistic atoms thus do not affect the result of the fit for the diffusion coefficients. Note that this is not the case after 50 ms as ballistic atoms are visible (see figure 2 [77]).

In addition to the investigation of the normal diffusion regime discussed above [77], we recently performed experiments with a lower temperature of 30 nK. In this case, equation (35)

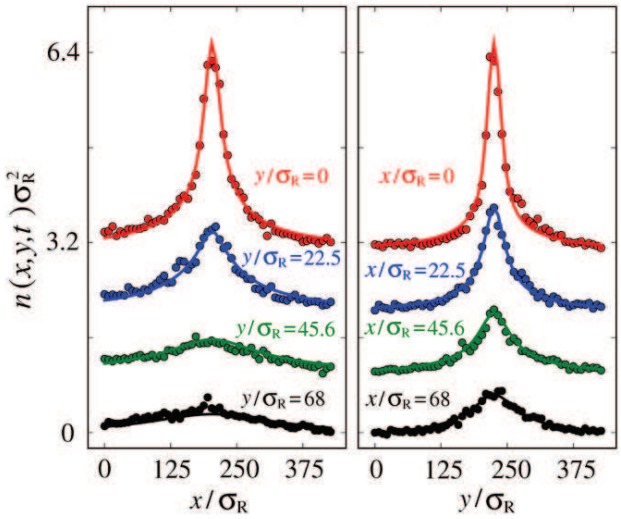

Figure 16. Experimental 2D column density distribution after 200 ms ($= 281\tau_R$) expansion of the atomic cloud. Dots are cuts along the x- (left panel) and y- (right panel) directions at cut positions explicitly indicated, artificially offset for clarity. Lines are the fitting function equation (36). Note that the spatial distribution is not Gaussian. This figure is reprinted from [77].

leads to 8% of classically trapped atoms and 55% of atoms in the sub-diffusive regime. We observe little expansion of the cloud as a function of time. For times of several seconds we observe losses due to residual heating. We are unable to quantitatively analyze the shape of the cloud because of the limited resolution of the imaging system and of the initial size of the cloud. The sub-diffusive regime and the percolation transition presented in this paper thus remain to be experimentally studied in 2D cold-atomic systems.

6. Conclusions

In this paper, we have studied the transport properties of a cold-atomic gas in a 2D anisotropic speckle potential, in the classical regime. We have shown that, upon proper rescaling, the atomic dynamics can be parameterized by the energy as the sole relevant quantity. Then, we have identified two asymptotically relevant regimes, depending on the particle energy: (i) for energy below the percolation threshold, any particle is trapped in a finite-size region, so that $\langle r^2 \rangle \to$ const (classical localization regime), along the $r = x, y$ direction. The probability of diffusion (defined as the average density probability of finding an atom at a given distance from its origin point) develops exponentially decaying tails, which correspond to the probability distribution of the size of the classically localized regions. Due to the pure topographical nature of the latter, the probability of diffusion is anisotropic with the same anisotropy factor as the speckle potential. (ii) For energy above the percolation threshold, there appear infinite-size allowed regions in which the gas expands diffusively, $\langle r^2 \rangle \propto t$ (normal diffusion regime). The probability of diffusion is a Gaussian function with anisotropy factor (along the x- and y-directions) significantly different from the anisotropic factor of the speckle potential. The diffusion coefficients along the two main directions of the speckle potential strongly depend on

the particle energy. More precisely, we found a power-law scaling, $D_r \sim E^\gamma$ with $\gamma \simeq 3.15$ for a blue-detuned speckle potential and $\gamma \simeq 3.45$ for a red-detuned speckle potential.

In addition, a transient sub-diffusion regime, where $\langle r^2 \rangle \propto t^{\alpha_r}$ with $\alpha_r < 1$, characterizes the dynamics at intermediate time scales, relevant to recent experiments [77]. This regime appears below and slightly above the percolation threshold. It is interpreted as due to the dynamics of exploration of finite-size allowed regions which are disconnected from each other or connected by narrow bottlenecks. For energy below the percolation threshold, the long-time dynamics crosses over to classical localization ($\alpha_r = 0$). Conversely, above the percolation threshold, it crosses over to normal diffusion ($\alpha_r = 1$). This example shows that sub-diffusion should not be regarded as a precursor of classical localization.

Using the above results as the groundwork, we have studied the expansion dynamics of a cloud of cold atoms with broad energy distributions, as relevant to recent experiments. First, we have calculated the energy distribution of the cloud in the presence of disorder. Then, we have discussed the dynamics. The time-dependent profiles are, in general, anisotropic and non-Gaussian, with tails governed by diffusive atoms. We have proposed a method to extract the energy-dependent diffusion coefficients from these tails, which involve many energy components. The experiments of [77] are realized in a quasi-2D geometry, which does not significantly change the above-discussed dynamics. The energy-dependent diffusion coefficients extracted from experimental data are in fair agreement with numerical calculations performed in the precise experimental geometry.

In future, it would be interesting to experimentally study the classical localization regime as discussed in the paper. In particular, working at lower temperature, it would be possible to create a gas of atoms with a significant fraction below the percolation threshold. Then, studying the fraction of classically localized atoms versus temperature, for instance, would give direct access to the percolation transition and, in particular, to the critical exponent. Another interesting direction would be to extend the study of transport in anisotropic 2D speckle potentials in the quantum regime, where traces of weak and strong localization effects can be searched for.

Acknowledgments

We thank Boris Shapiro for useful comments on the manuscript and M Besbes for assistance on numerical calculations. This work was supported by CNRS, CNES as part of the ICE project, Direction Générale de l'Armement, the European Research Council (FP7/2007-2013; grant agreement no. 256294), Agence Nationale de la Recherche (contract no. ANR-08-blan-0016-01), RTRA Triangle de la Physique, IXSEA, the EuroQuasar program of the EU and the MAP program SAI of the European Space Agency. LCFIO is a member of Institut Francilien de Recherche sur les Atomes Froids. We acknowledge the use of the computing facility cluster GMPCS of the LUMAT Federation (FR LUMAT 2764).

References

[1] Lee P A and Ramakrishnan T V 1985 *Rev. Mod. Phys.* **57** 287
[2] Reppy J D 1992 *J. Low Temp. Phys.* **87** 205
[3] Akkermans E and Montambaux G 2007 *Mesoscopic Physics of Electrons and Photons* (Cambridge: Cambridge University Press)
[4] John S 1991 *Phys. Today* **44** 32

[5] Chandrasekhar S 1960 *Radiative Transfer* (New York: Dover)
[6] Ashcroft N W and Mermin N D 1976 *Solid State Physics* (Philadelphia, PA: Saunders)
[7] Vollhardt D and Wölfle P 1980 *Phys. Rev.* B **22** 4666
[8] Anderson P W 1958 *Phys. Rev.* **109** 1492
[9] de Gennes P-G 1966 *Superconductivity of Metals and Alloys* (New York: Benjamin)
[10] Mott N F 1968 *Rev. Mod. Phys.* **40** 677
[11] Mott N F 1990 *Metal-Insulator Transitions* (London: Taylor and Francis)
[12] Vollhardt D and Wölfle P 1992 *Electronic Phase Transitions* ed W Hanke and Y V Kopaev (Amsterdam: Elsevier)
[13] Fallani L, Fort C and Inguscio M 2008 *Adv. At. Mol. Opt. Phys.* **56** 119
[14] Sanchez-Palencia L and Lewenstein M 2010 *Nature Phys.* **6** 87
[15] Modugno G 2010 *Rep. Prog. Phys.* **73** 102401
[16] Lagendijk A, van Tiggelen B A and Wiersma D S 2009 *Phys. Today* **62** 24
[17] Aspect A and Inguscio M 2009 *Phys. Today* **62** 30
[18] Dalfovo F, Giorgini S, Pitaevskii L P and Stringari S 1999 *Rev. Mod. Phys.* **71** 463
[19] Giorgini S, Pitaevskii L P and Stringari S 2008 *Rev. Mod. Phys.* **80** 1215
[20] Lewenstein M, Sanpera A, Ahufinger V, Damski B, Sen(De) A and Sen U 2007 *Adv. Phys.* **56** 243
[21] Bloch I, Dalibard J and Zwerger W 2008 *Rev. Mod. Phys.* **80** 885
[22] Clément D, Varón A F, Retter J A, Sanchez-Palencia L, Aspect A and Bouyer P 2006 *New J. Phys.* **8** 165
[23] Damski B, Zakrzewski J, Santos L, Zoller P and Lewenstein M 2003 *Phys. Rev. Lett.* **91** 080403
[24] Roth T and Burnett K 2003 *J. Opt. B: Quantum Semiclass. Opt.* **5** S50
[25] Gavish U and Castin Y 2005 *Phys. Rev. Lett.* **95** 020401
[26] Kuhn R C, Miniatura C, Delande D, Sigwarth O and Müller C A 2005 *Phys. Rev. Lett.* **95** 250403
[27] Massignan P and Castin Y 2006 *Phys. Rev.* A **74** 013616
[28] Sanchez-Palencia L, Clément D, Lugan P, Bouyer P, Shlyapnikov G V and Aspect A 2007 *Phys. Rev. Lett.* **98** 210401
[29] Kuhn R C, Sigwarth O, Miniatura C, Delande D and Müller C A 2007 *New. J. Phys.* **9** 161
[30] Skipetrov S E, Minguzzi A, van Tiggelen B A and Shapiro B 2008 *Phys. Rev. Lett.* **100** 165301
[31] Miniatura C, Khun R C, Delande D and Müller C A 2009 *Eur. Phys. J.* B **68** 353
[32] Pezzé L, Hambrecht B and Sanchez-Palencia L 2009 *Europhys. Lett.* **88** 30009
[33] Pezzé L and Sanchez-Palencia L 2011 *Phys. Rev. Lett.* **106** 040601
[34] Antezza M, Castin Y and Hutchinson D 2010 *Phys. Rev.* A **82** 043602
[35] Piraud M, Lugan P, Bouyer P, Aspect A and Sanchez-Palencia L 2011 *Phys. Rev.* A **83** 031603
[36] Bilas N and Pavloff N 2006 *Eur. Phys. J.* D **40** 387
[37] Lugan P, Clément D, Bouyer P, Aspect A, Lewenstein M and Sanchez-Palencia L 2007 *Phys. Rev. Lett.* **98** 170403
[38] Lugan P, Clément D, Bouyer P, Aspect A and Sanchez-Palencia L 2007 *Phys. Rev. Lett.* **99** 180402
[39] Lugan P and Sanchez-Palencia L 2011 *Phys. Rev.* A **84** 013612
[40] Paul T, Schlagheck P, Leboeuf P and Pavloff N 2007 *Phys. Rev. Lett.* **98** 210602
[41] Horstmann B, Cirac J I and Roscilde T 2007 *Phys. Rev.* A **76** 043625
[42] Roux G, Barthel T, McCulloch I P, Kollath C, Schollwoeck U and Giamarchi T 2008 *Phys. Rev.* A **78** 023628
[43] Paul T, Albert M, Schlagheck P, Leboeuf P and Pavloff N 2009 *Phys. Rev.* A **80** 033615
[44] Orso G, Iucci A, Cazalilla M A and Giamarchi T 2009 *Phys. Rev.* A **80** 033625
[45] Falco G M, Nattermann T V and Pokrovsky L 2009 *Europhys. Lett.* **85** 30002
[46] Pollet L, Prokof'ev N V, Svistunov B V and Troyer M 2009 *Phys. Rev. Lett.* **103** 140402
[47] Aleiner I L, Altshuler B L and Shlyapnikov G V 2010 *Nature Phys.* **6** 900
[48] Orso G 2007 *Phys. Rev. Lett.* **99** 250402
[49] Byczuk K, Hofstetter W and Vollhardt D 2009 *Phys. Rev. Lett.* **102** 146403
[50] Byczuk K, Hofstetter W and Vollhardt D 2010 *Int. J. Mod. Phys.* B **24** 1727

[51] Han L and Sá de Melo C A R 2011 *New J. Phys.* **13** 055012
[52] Sanpera A, Kantian A, Sanchez-Palencia L, Zakrewski J and Lewenstein M 2004 *Phys. Rev. Lett.* **93** 040401
[53] Ahufinger V, Sanchez-Palencia L, Kantian A, Sanpera A and Lewenstein M 2005 *Phys. Rev.* A **72** 063616
[54] Wehr J, Niederberger A, Sanchez-Palencia L and Lewenstein M 2006 *Phys. Rev.* B **74** 224448
[55] Niederberger A, Schulte T, Wehr J, Lewenstein M, Sanchez-Palencia L and Sacha K 2008 *Phys. Rev. Lett.* **100** 030403
[56] Niederberger A, Wehr J, Lewenstein M and Sacha K 2009 *Europhys. Lett.* **86** 26004
[57] Niederberger A, Rams M M, Dziarmaga J, Cucchietti F M, Wehr J and Lewenstein M 2010 *Phys. Rev.* A **82** 013630
[58] Crépin F, Zaránd G and Simon P 2010 *Phys. Rev. Lett.* **105** 115301
[59] Clément D, Varón A F, Hugbart M, Retter J A, Bouyer P, Sanchez-Palencia L, Gangardt D M, Shlyapnikov G V and Aspect A 2005 *Phys. Rev. Lett.* **95** 170409
[60] Fort C, Fallani L, Guarrera V, Lye J E, Modugno M, Wiersma D S and Inguscio M 2005 *Phys. Rev. Lett.* **95** 170410
[61] Billy J, Josse V, Zuo Z, Bernard A, Hambrecht B, Lugan P, Clément D, Sanchez-Palencia L, Bouyer P and Aspect A 2008 *Nature* **453** 891
[62] Roati G, D'Errico C, Fallani L, Fattori M, Fort C, Zaccanti M, Modugno G, Modugno M and Inguscio M 2008 *Nature* **453** 895
[63] Deissler B, Zaccanti M, Roati G, D'Errico C, Fattori M, Modugno M, Modugno G and Inguscio M 2010 *Nature Phys.* **6** 354
[64] Lucioni E, Deissler B, Tanzi L, Roati G, Zaccanti M, Modugno M, Larcher M, Dalfovo F, Inguscio M and Modugno G 2011 *Phys. Rev. Lett.* **106** 230403
[65] White M, Pasienski M, McKay D, Zhou S Q, Ceperley D and DeMarco B 2009 *Phys. Rev. Lett.* **102** 055301
[66] Pasienski M, McKay D, White M and DeMarco B 2010 *Nature Phys.* **6** 677
[67] Bouchaud J P and Georges A 1990 *Phys. Rep.* **195** 127
[68] van Rossum M C W and Nieuwenhuizen Th M 1999 *Rev. Mod. Phys.* **71** 313
[69] Rammer J 1998 *Quantum Transport Theory* (Reading, MA: Perseus Books)
[70] Kramer B and MacKinnon A 1993 *Rep. Prog. Phys.* **56** 1569
[71] Abrahams E, Anderson P W, Licciardello D C and Ramakrishnan T V 1979 *Phys. Rev. Lett.* **42** 673
[72] Hartung M, Wellens T, Müller C A, Richter K and Schlagheck P 2008 *Phys. Rev. Lett.* **101** 020603
[73] Horak P, Courtois J-Y and Grynberg G 1998 *Phys. Rev.* A **58** 3953
[74] Grynberg G, Horak P and Mennerat-Robilliard C 2000 *Europhys. Lett.* **49** 424
[75] Shapiro B 2007 *Phys. Rev. Lett.* **99** 060602
[76] Beilin L, Gurevich E and Shapiro B 2010 *Phys. Rev.* A **81** 033612
[77] Robert-de-Saint-Vincent M, Brantut J-P, Allard B, Plisson T, Pezzé L, Sanchez-Palencia L, Aspect A, Bourdel T and Bouyer P 2010 *Phys. Rev. Lett.* **104** 220602
[78] Clément D, Bouyer P, Aspect A and Sanchez-Palencia L 2008 *Phys. Rev.* A **77** 033631
[79] Chen Y P, Hitchcock J, Dries D, Junker M, Welford C and Hulet R G 2008 *Phys. Rev.* A **77** 033632
[80] Dries D, Pollack S E, Hitchcock J M and Hulet R G 2010 *Phys. Rev.* A **82** 033603
[81] Goodman J W 2006 *Speckle Phenomena in Optics* (Englewood Cliffs, NJ: Roberts)
[82] Zallen R and Scher H 1971 *Phys. Rev.* B **4** 4471
[83] Isichenko M B 1992 *Rev. Mod. Phys.* **64** 961
[84] Smith L N and Lobb C J 1979 *Phys. Rev.* B **20** 3653
[85] Weinrib A 1982 *Phys. Rev.* B **26** 1352
[86] Metzler R and Klafter J 2000 *Phys. Rep.* **339** 1
[87] Lugan P, Aspect A, Sanchez-Palencia L, Delande D, Grémaud B, Müller C A and Miniatura C 2009 *Phys. Rev.* A **80** 023605
[88] Gurevich E and Kenneth O 2009 *Phys. Rev.* A **79** 063617
[89] Lifshits I M, Gredeskul S A and Pastur L A 1988 *Introduction to the Theory of Disordered Systems* (New York: Wiley)

[90] Klages R, Radons G and Sokolov I M 2008 *Anomalous Transport* (New York: Wiley)
[91] Bathelemy P, Bertolotti J and Wiersma D 2008 *Nature* **453** 495
[92] Mercadier N, Guerin W, Chevrollier M and Kaiser R 2009 *Nature Phys.* **5** 602
[93] Bardou F, Bouchaud J P, Emilie O, Aspect A and Cohen-Tannoudji C 1994 *Phys. Rev. Lett.* **72** 203
[94] Sanchez-Palencia L, Horak P and Grynberg G 2002 *Eur. Phys. J.* D **18** 353
Sanchez-Palencia L and Grynberg G 2003 *Phys. Rev.* A **68** 023404
[95] Cherroret N and Skipetrov S E 2008 *Phys. Rev. Lett.* **101** 190406
[96] Cherroret N and Skipetrov S E 2009 *Phys. Rev.* A **79** 063604
[97] Pilati S, Giorgini S, Modugno M and Prokof'ev N 2010 *New J. Phys.* **12** 073003